Sting jets: unravelling the impact of conditional symmetric instability, evaporation and frontolysis in the St. Jude's Day storm

Author: Yannick Damen; Supervisors: Gert-Jan Steeneveld and Leo Kroon

November 13, 2017

Abstract

High wind speeds associated with extratropical cyclones cause large damages and several casualties per year in Western Europe. Sting jets, mesoscale jets occurring south-east of the low-pressure core, account for part of the damages. When sting jet momentum is transported to the surface, wind gusts can be severe. This study looked at the influence of three important factors on sting jets: evaporation, conditional symmetric instability (CSI) and frontolysis. A WRF case study has been conducted on the evolution of sting jets and latter factors during the life cycle of the St. Jude's Day storm of 28 October 2013. It was found that several sting jets occurred during the phase of rapid cyclogenesis. Furthermore, evaporation was found to be the most important influence during the first phase of sting jets, followed by CSI. The importance of evaporation decreased during the progression of the storm, whereas the importance of CSI increased. The relative importance of frontolysis was unclear and needs to be assessed in future research.

Contents

1 Introduction

High wind speeds related to extratropical cyclones account for 3.5 Billion Euro in damages per year in Europe alone (Barredo, 2010; Schultz & Browning, 2017). Sting jets account for a part of this number. Due to climate change, it is expected that losses will increase and it is therefore important to model extratropical cyclones and sting jets (e.g. (Leckebusch & Ulbrich, 2004; Schwierz et al., 2010; Donat et al., 2011)). Several conceptual models for the representation of extratropical cyclones have been proposed during the preceding century, of which the Norwegian School Model, Conveyor Belt Model and Shapiro-Keyser Model are the most renowned (Bjerknes, 1919; Carlson, 1980; Shapiro & Keyser, 1990; Schultz, 2001; Schultz & Vaughan, 2010). Although all these models seem to represent extratropical cyclones and their dynamics rather well, some distinct features still do not match the expected. Several authors found high wind speeds and gusts outside the cold conveyor belt region and named this feature "sting jet" (Figure 4 and 5) (Grønås, 1995; Browning, 2004; Clark et al., 2005). In the years following the papers of Browning (2004) and Clark et al. (2005), extensive research on sting jets has been conducted (e.g. Gray et al. (2011); Martínez-Alvarado et al. (2012); Schultz & Sienkiewicz (2013); L. H. Baker et al. (2014); Browning et al. (2015); Coronel et al. (2016)). Their research mainly focused on factors influencing the genesis of sting jets in both idealised studies as well as case studies of real storms.

Browning (2004) hypothesized that evaporation at the end of the cloud head could be a mechanism of bringing air from aloft to lower levels and even to the surface. He furthermore hypothesized Conditional Symmetric Instability (CSI) to be a factor playing a role in downdraught air parcels in a sting jet. Schultz & Sienkiewicz (2013) proposed a physical explanation for the location of a sting jet denoting that CSI and evaporation would play a minor role in the genesis of a sting jet and could be regarded as subsequent features of frontolysis: the dissipation of a front in a region of diverging isentropes. This break-apart dynamics of the bent-back occlusion would be the leading factor in producing evaporation, CSI and subsequent downward motions of air trajectories in the sting jet region (Schultz & Sienkiewicz, 2013).

During the last couple of years, several articles have been published which, in a sense, seem to oppose each others findings. For instance, Browning (2004) and Browning et al. (2015) state that evaporation is a major factor in bringing sting jet momentum downwards, though L. H. Baker et al. (2014) found that turning off evaporation in a model run had no effect on the simulated sting jet. Others found CSI being a major factor in producing and bringing high-momentum sting jet air down from aloft (e.g. Martínez-Alvarado et al. (2012); Gray et al. (2011); L. H. Baker et al. (2014)). Schultz & Sienkiewicz (2013) and Coronel et al. (2016) proposed neither evaporation, nor CSI are the main factors in producing a sting jet.

As such, it seems as if some kind of chicken and egg problem exists: it is not exactly known which process initiates a sting jet and subsequent features. Furthermore, the relative importance of the three main factors (evaporation, CSI and frontolysis dynamics) is not known.

This research has looked into the sequence of events leading to a sting jet and the relative importance of the three main factors. This has been assessed in a case study on the St. Jude's Day storm of 28 October 2013 using the following research questions:

1. *How do the sting jet forming factors Conditional Symmetric Instability (CSI), evaporation and frontal dynamics in the sting jet region change during the development of a Shapiro-Keyser type extratropical cyclone?*
    - *Which trajectories do air parcels follow before entering the sting jet region?*
    - *Which areas on the south side of the low pressure centre show CSI?*
    - *How much evaporation is taking place in the sting jet region?*
    - *How much frontolysis is taking place in the sting jet region*
2. *What is the interaction of Conditional Symmetric Instability (CSI), evaporation and frontal dynamics in the sting jet region?*

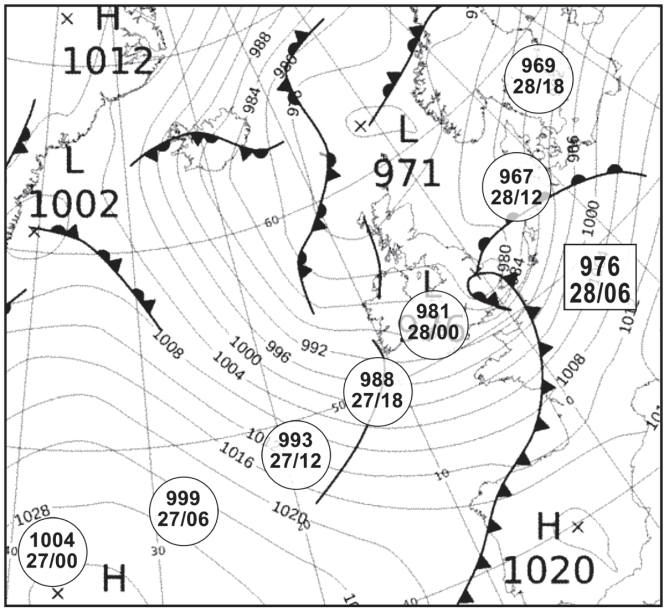

Figure 1: Track of the St. Jude's Day storm. Note the rapid drop in pressure from 993 hPa to 967 hPa in just one day. (Browning et al., 2015)

The St. Jude's Day storm has already been studied by Browning et al. (2015) and has been confirmed to produce a sting jet.

The low pressure system originated from the northern Atlantic ocean and deepened rapidly as it swung across Western-Europe (26 hPa in 24 h) (Figure 1) (Browning et al., 2015). Damage was large along the track of the area south of the low pressure centre. Furthermore, very strong wind gusts have been reported, for instance 151 km/h in the Netherlands and 193 km/h in Denmark (KNMI and DMI, 2013). The storm showed evaporating cloud filaments, which are clear features of a sting jet (Figure 6) (Browning et al., 2015).

2 Background

2.1 Shapiro-Keyser cyclones

Opposed to the Norwegian school of extratropical cyclones, Shapiro & Keyser (1990) found a different type of extratropical cyclone which will be referred to as a Shapiro-keyser cyclone.

There exist four phases in the development of Shapiro-keyser cyclones (Figure 3). 1) The birth of a cyclone out of a front. 2) The formation of a frontal fracture. 3) The cold front aligning itself perpendicular to the warm front (frontal T-bone); formation of the bent-back warm front. 4) Warm core seclusion. In this stage, the extratropical cyclone is fully developed (Shapiro & Keyser, 1990).

The first two phases are rather similar to Norwegian school model cyclones (2, though the only difference is the cold front being perpendicular to the warm front in the Shapiro-Keyser model. In this model, the cold front is de-

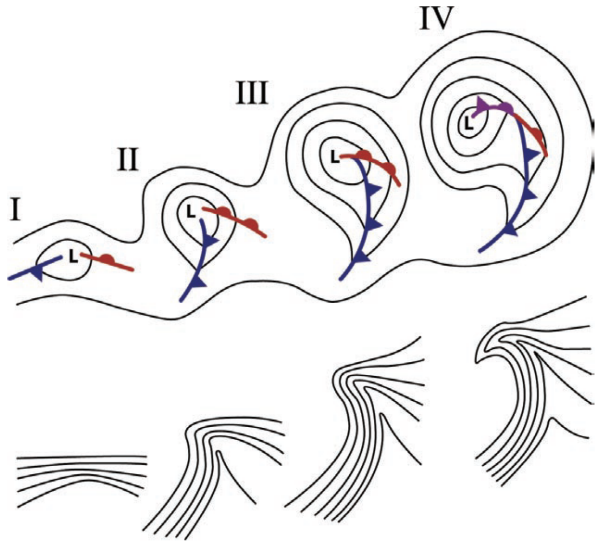

Figure 2: Norwegian school conceptual model of an extratropical cyclone. The Roman numbers indicate the stages of development. The black contours in the upper figure indicate geopotential lines; the black contours in the lower figure show potential temperature. During its development, the cold and warm front wrap around the low pressure centre as an occluded front. (Schultz & Vaughan, 2010)

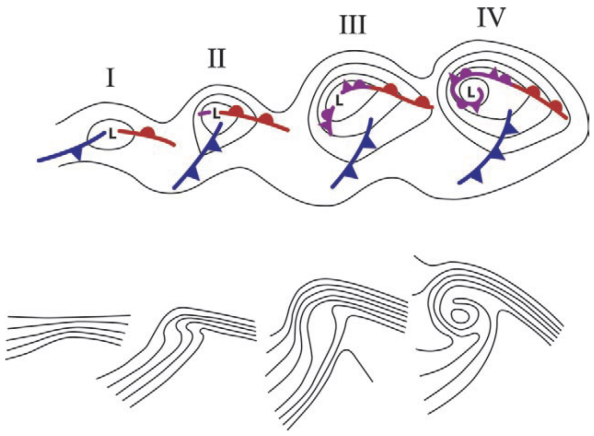

Figure 3: Conceptual model developed by Shapiro and Keyser (1990). The Roman numbers depict different stages of development. The black contours are similar to figure 1. The cold front is detached from the warm front forming a frontal fracture. The warm front wraps around the low pressure centre as an occluded front, dragging warm air into the core and thus creating a warm-core seclusion. (Schultz & Vaughan, 2010)

tached from the warm front due to differential rotation, leading to the front being weaker and thus looks fractured (Browning et al., 1997; Schultz et al., 1998). As a result, there is no narrowing tongue of warm air as in the Norwegian model and no wrap-up will take place (Schultz & Vaughan, 2010).

Although this does not lead to an occlusion process similar to the Norwegian school model, the distance between the warm sector and the core of the cyclone will increase in stages three and four (Schultz & Vaughan, 2010).

Another feature of the final stages is warm air (which can freely flow into the centre of low pressure due to the frontal fracture) being entrapped in the low pressure centre, bordered by cooler air (warm-core seclusion).

Furthermore, the warm front wraps around the cyclones' core as a bent-back occlusion (though not being a traditional occlusion as defined in the Norwegian model) (Shapiro & Keyser, 1990; Schultz et al., 1998; Schultz & Vaughan, 2010).

Extratropical cyclones of this kind are rapidly developing and fast moving systems. They are able to form sting jets in stage two and three, whereas none will form in Norwegian school cyclones (Browning, 2004; Clark et al., 2005; Martínez-Alvarado et al., 2012).

This makes the distinction these two different kinds of extratropical cyclones an important one, as we want to know when sting jets occur. In that sense, we can just focus on Shapiro-Keyser type extratropical cyclones.

2.2 Sting jets

Sting jets were defined by Browning (2004) and Clark et al. (2005) as air parcels which 'descended and accelerated down to the surface in a discrete mesoscale jet' (Clark et al., 2005). They are located at the southern tip of the cloud head, outside the cold conveyor belt (CCB) and occur in phase two and three of the Shapiro-Keyser model of extratropical cyclones (Figure 4) (Clark et al., 2005). When looking at a flow-following cross section (Figure 5), sting jets follow descending trajectories, lying above the CCB jet, but below the dry intrusion. They are often characterized by evaporating cloud filaments, which are sometimes visible on satellite images (Figure 6) and may produce damaging wind gusts at the end of these filaments (Browning et al., 2015). In the years following the articles of Browning (2004) and Clark et al. (2005) many case studies have been conducted, as well as idealized studies. Case studies focussed on major storms, for instance the 1987 Great Storm (Browning, 2004; Clark et al., 2005), windstorm Jeanette (27 October 2002) (Parton et al., 2009), Windstorm Gudrun / Erwin (7 January 2005) (L. Baker, 2009) and windstorm Anna (26 February 2002) (Martínez-Alvarado et al., 2010). The idealized studies focussed on modelling sting jets in the best possible manner, trying to provide a physical mechanism or to come up with factors playing a role in the development of a sting jet (e.g. L. H. Baker et al. (2014); Coronel et al. (2016)). Important factors playing a role in the genesis of a sting jet were found to be evaporation (Browning, 2004; Clark et al., 2005; Browning et al., 2015)), Conditional Symmetric Instability (e.g. Browning (2004); Clark et al. (2005); Parton et al. (2009); Gray et al. (2011); L. H. Baker et al. (2014) and general dynamic (geostrophic) forcings

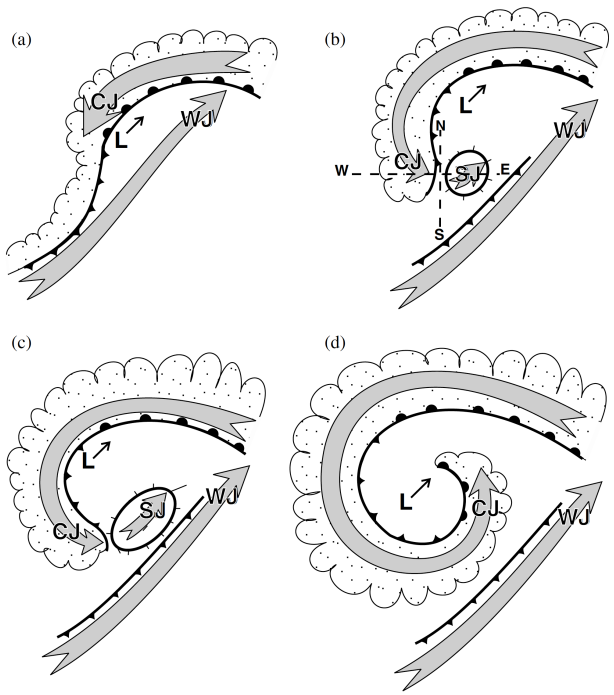

Figure 4: Different stages in the development of a sting jet. WJ depicts the warm conveyor belt jet, CJ the cold conveyor belt jet and SJ is the sting jet. The L denotes the low pressure centre. The SJ develops in figure b in between the tip of the cloud head and the fractured cold front. During stage c, the occluded bent-back front wraps around the low pressure centre further, pushing the SJ further from the core of the depression. The SJ disappears in stage d due to the extensive wrap-around of the occlusion. (Clark et al., 2005)

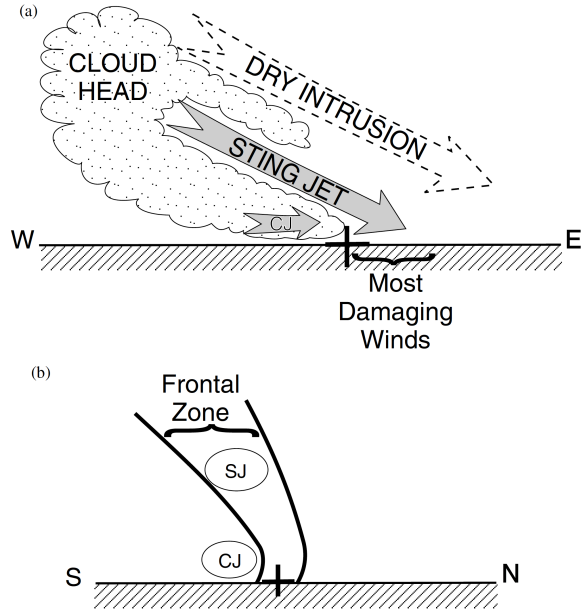

Figure 5: Vertical cross-section of a sting jet trajectory along the front(a) and perpendicular (b). The sting jet (SJ) originates from the cloud head, being beneath the dry intrusion and above the cold conveyor belt jet (CJ). (Clark et al., 2005)

(Schultz & Sienkiewicz, 2013; Coronel et al., 2016). These so-called 'main' factors will be explained in the next sections.

2.2.1 Evaporation

It has been proposed that evaporation could lead to cooling of the surrounding air. In sting jet trajectories, Clark et al. (2005) found an overall decrease in potential temperature, on average being 0.7 K with a maximum of 8 K. Moreover, the relative humidity decreased from almost 100 % to on average 50 % and even up to 30 % in more extreme trajectories. During their descent, the potential wet bulb temperature of the air parcels in the sting jet was conserved. This led to the conclusion that the air parcels descended among others due to evaporation (Clark et al., 2005). In most cases, this air stream does not reach the surface. However, in the presence of convection, some of this high-momentum air can be transported to ground level, leading to strong wind gusts (Browning et al., 2015). These surface-reaching swaths of air are only visible in some localised showers, though also in the absence of convection some sting jet related wind gusts may occur (Browning et al., 2015).

To calculate the amount of evaporation, the difference between the mixing ratios for dry and wet adiabatically descended air parcel can be used. The latter can be assessed by looking at a skew-T log-p diagram, starting at for instance 700 hPa and following the dry adiabat downwards for the 'dry' parcel and the wet adiabat for the 'wet' parcel. The difference between mixing ratios at the surface can than be regarded as the total amount of evaporated water. It is assumed that no precipitation occurs near and inside the air parcel and that the air is just saturated, thus not super-saturated.

Another way to assess the amount of evaporation is to do a real calculation instead of using skew-T log-p diagrams. This calculation involves the first law of thermodynamics which is defined as follows:

$$dq = c_p dT - \frac{1}{\rho} dp + L_v dq_s \tag{1}$$

Where q is the specific heat energy, c_p the specific heat capacity of dry air at constant pressure, T is temperature, ρ is the density of air, p is the air pressure, L_v is the latent heat of vaporization and q_s is the water saturation specific humidity. Since the descending motion in a sting jet is assumed to be adiabatic, $dq = 0$. As such, equation 1 can be rewritten as follows:

$$\frac{L_v}{c_p} dq_s = \frac{1}{\rho c_p} dp - dT \tag{2}$$

$$dq_s = \frac{1}{L_v \rho} dp - \frac{c_p}{L_v} dT \tag{3}$$

It is assumed in this equation that all evaporated water remains inside the air parcel during descent, making it a

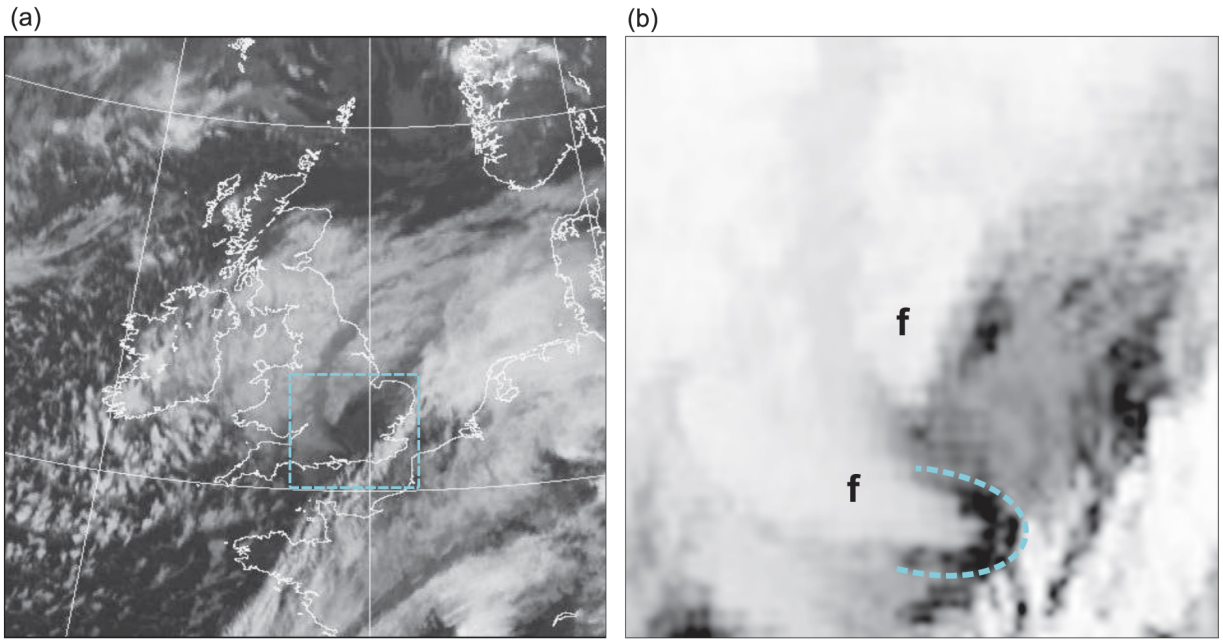

Figure 6: Rectified MSG (Meteosat Second Generation) IR image at 28 October 2013, 0600 UTC. Figure (a) shows the developing cyclone. Figure (b) is zoomed in from (a) (matching the blue dashed box over South-Eastern England). The letters 'f' denote the evaporating cloud filaments and sting jets. The dark areas at the edges of these cloud filaments show very low relative humidity. (Image courtesy and copyright EUMETSAT/Dundee Satellite Receiving Station) (Browning et al., 2015)

reversible adiabatic process. It is moreover assumed that no precipitation occurs. Note that this equation only applies for liquid water and thus not for ice. Because sting jet air also contains frozen particles, the phase change from ice to water vapour should be incorporated as well. This can be done by changing the latent heat of vaporization (L_v) into the latent heat of sublimation (L_s) in equation 3. This implies that the relative amount of ice particles and water in sting jet air should be known.

Summarizing, possible ways to determine whether evaporation plays a role in the sting jet region, one could look at relative humidity, potential temperature change and conservation of potential wet bulb temperature. To assess the amount of evaporated water, one could look at thermodynamic diagrams and perform a calculation with the first law of thermodynamics.

2.2.2 CSI

There are more ways of bringing high-momentum air down from aloft besides cooled pockets of air which are colder than the environment. If the air is unstable, mixing can occur, since upwards moving air needs to be counteracted by downwards moving air. In the case of large scale systems, large areas of ascending motions and large areas of descending motions can be discerned. In the case of convection in the boundary layer, eddies are much smaller leading to localised ascending and descending pockets of air.

In the case of sting jets, high-momentum air can only be brought down from aloft when the environment is conditionally symmetrically unstable. The latter means that the air is stable for both horizontal and vertical motions, however, in case of slantwise movement, the air becomes unstable (Gray et al., 2011). The result of this process is convection being produced, leading to mixing and as such descending motions of high-momentum air. Proxies for CSI are Downdraught Slantwise Convective Available Potential Energy (DSCAPE) and its sister Slantwise Convective Available Potential Energy (SCAPE). The former relates to energy being released within downwards moving air parcels, whereas the latter is applied to upward moving air parcels (Gray et al., 2011)). Both are a measure of the maximum kinetic energy available to an ascending air parcel within a conditionally symmetrically unstable environment (Gray et al., 2011). CAPE can be calculated using the following formula:

$$CAPE = \int_{pLNB}^{p0} R_d(T_{v,parcel} - T_{v,env}) d\ln(p) \qquad (4)$$

Where R_d is the gas constant for dry air, $T_{v,parcel}$ and $T_{v,env}$ are the virtual temperatures for the air parcel and environment respectively. The integration limits $pLNB$ and $p0$ denote the pressure at a level of neutral buoyancy and the pressure at the origin. T_v can be calculated as follows:

$$T_v = T\frac{(1 + r/\epsilon)}{(1 + r)} \qquad (5)$$

Where r is the mixing ratio and ϵ is the ratio of the gas constants of dry and moist air.

SCAPE is calculated like CAPE, but along an absolute momentum surface M. For the horizontal (so in case of two dimensions), M and N are defined as follows:

$$M = fx + v \tag{6}$$

Where f is the coriolis parameter ($2\Omega \sin(\phi)$), x is the distance in the x-direction and v is the wind speed in the y-direction. Similarly:

$$N = fy - u \tag{7}$$

Where f is again the coriolis parameter, y is the distance in the y-direction and u is the wind speed in the x-direction.

In case of sting jets, we need to look in three dimensions. In that case, the absolute momentum surface is calculated as the surface where the two horizontal components of absolute momentum (equations 6 and 7) intersect with the air parcel's initial position (Shutts, 1990).

If SCAPE is present in a certain area and CAPE is (almost) absent, this is an indication of CSI. If SCAPE decreases over time, it could indicate the release of CSI (Gray et al., 2011). Slantwise CAPE provides an accurate visualisation and quantification of areas with CSI and associated slantwise convection. However, SCAPE is rather difficult to calculate in a 3D model field (Gray et al., 2011).

An easier measure which is frequently used in sting jet analyses is Saturated Moist Potential vorticity MPV^* which is defined as follows:

$$MPV^* = \frac{1}{\rho}\zeta \cdot \nabla\theta_e^* \tag{8}$$

Where ρ is density, ζ is relative vorticity and θ_e^* is the saturated equivalent potential wet bulb temperature. θ_e^* is definded as follows:

$$\theta_e^* = \theta \exp\left(\frac{L_v q_s}{c_p T}\right) \tag{9}$$

When MPV^* is negative and the environment is conditionally and inertially stable, it indicates that CSI exists (Gray et al., 2011).

Release of CSI can only take place in a saturated environment, which is already incorporated in θ_e^* (L. H. Baker et al., 2014). One could discriminate between regions which favour the release of CSI by applying a certain threshold to relative humidity. L. H. Baker et al. (2014) have used such a criterion and set it to $RH > 90\%$. They've used these conditions to determine where CSI may be present.

2.2.3 Dynamical forcing

The previous subsections related to mesoscale processes and proxies. This subsection will focus more on synoptic scale processes which could influence sting jets or general descending motions.

In the case of Shapiro-Keyser cyclones, the end of the bent-back occluded front is marked by an area of diverging isentropes. This feature is indicative for so-called frontolysis: the dissipation of fronts. Opposed to frontogenesis, which literally means the birth of a front, in frontolysis fronts break apart (Figure 7) (Schultz & Sienkiewicz, 2013).

Schultz & Sienkiewicz (2013) have used Petterssen (1936) frontogenesis as an easy method to determine the areas of frontogenesis and frontolysis. Petterssen frontogenesis is defined as the time rate of change of the magnitude of the horizontal gradient of potential temperature (equation 10).

$$F = \frac{d}{dt}|\nabla_H \theta| \tag{10}$$

In which $\frac{d}{dt}$ can be written out as

$$\frac{d}{dt} = \frac{\partial}{\partial t} + u\frac{\partial}{\partial x} + v\frac{\partial}{\partial y}$$

and $|\nabla_H \theta|$ as

$$|\nabla_H \theta| = \frac{\partial \theta}{\partial x} + \frac{\partial \theta}{\partial y}$$

Petterssen (1936) moreover showed that this equation could be written in terms of divergence and deformation (equation 11):

$$F = \frac{1}{2}|\nabla_H|(E\cos(2\beta) - \nabla_{\mathbf{H}} \cdot \mathbf{V_H}) \tag{11}$$

Where E is deformation and β is the angle between an isentrope and the axis of dilatation (which is defined as a line along which deformation of the airflow is causing the maximum stretching of air parcels) (Cohen & Schultz, 2005; Schultz & Sienkiewicz, 2013). Negative values of F indicate frontolysis, whereas positive values indicate frontogenesis (Petterssen, 1936; Schultz & Sienkiewicz, 2013).

These equations can, however, only be applied in horizontal flow. Since a sting jet is purely three dimensional, (Coronel et al., 2016) used (the divergence of) Q-vectors (defined by Hoskins et al. (1978)) to develop a dynamic framework explaining the genesis of sting jets. These are defined as follows:

$$\mathbf{Q} = \frac{g}{\theta_0}\left[\left(\frac{\partial \mathbf{u_g}}{\partial x}\right) \cdot \nabla\theta, \left(\frac{\partial \mathbf{v_g}}{\partial y}\right) \cdot \nabla\theta\right] \tag{12}$$

In which θ is the potential temperature, θ_0 is the potential temperature at the surface and $\mathbf{u_g}$ and $\mathbf{v_g}$ are the geostrophic wind components. Frontolysis occurs in case of diverging Q-vectors and frontogenesis in case of converging Q-vectors (Coronel et al., 2016). Coronel et al. (2016) found that the cross-front component of the Q-vector was non-negligible, however, the along-front component was dominant in creating divergence. This would support the results of Schultz & Sienkiewicz (2013), but due to the along-front component it would be necessary to visualize the Q-vector and its divergence in three dimensions. When using the latter approach, the descent in the sting jet region could be explained better.

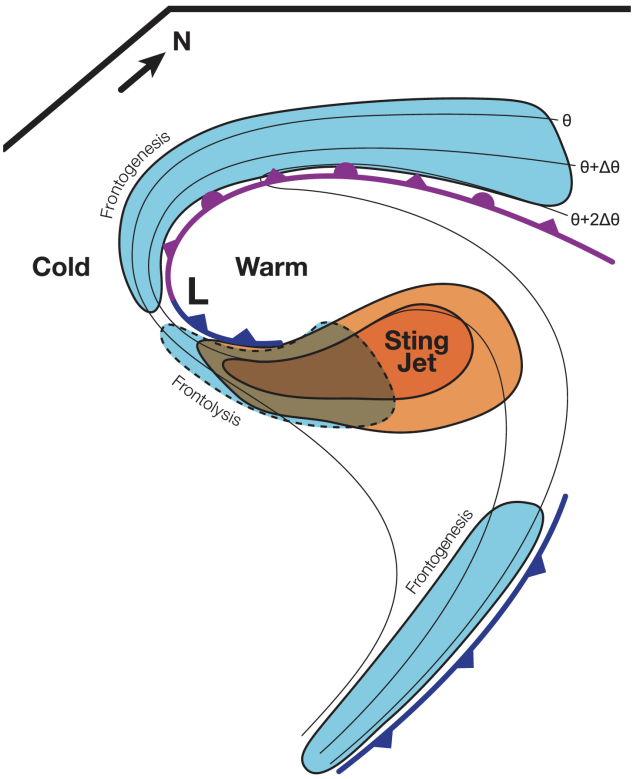

Figure 7: Conceptual model developed by Schultz & Sienkiewicz (2013) concerning the impact of frontloysis on a sting jet. The orange shaded part depicts the sting jet, the blue shaded parts show frontogenesis (full black line) and frontolysis (dashed black line). The other, thin contours show isentropes. The sting jet occurs in the region of frontolysis. (Schultz & Sienkiewicz, 2013)

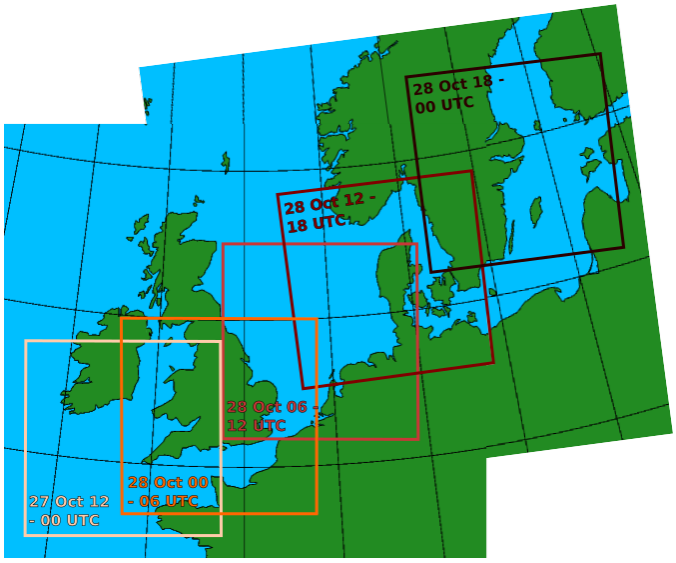

Figure 8: Model domain. The mother domain has 200 x 180 grid cells and its horizontal resolution is 9 km. The inner domains have 241 x 241 grid cells and a horizontal resolution is 3 km. The different inner domains denote manually moved nests, reinitialised every six hours.

3 Methods

This section will provide and explain the steps which will be used in this research. The first subsection will introduce WRF and explain the model configuration for this particular research. The second subsection will walk through the research- and sub-questions and explains the steps which will be conducted.

3.1 Initialising WRF and parametrisations

WRF-ARW version 3.7.1 has been used to model the sting jet behaviour in the St. Jude's Day storm (Skamarock & Klemp, 2008). The model set-up was similar to Browning et al. (2015), since they already successfully modelled the same case in WRF.

Model initialisation has been done with ECMWF data every six hours, starting from 27 October, 12 UTC and ending 29 October 12 UTC, spanning a total of 48 hours. The latter initialisaton data set has a horizontal resolution of 25 km and contains 26 vertical levels. For every run, the spin-up time is approximately 6 hours. This method has been chosen since numerous model runs conducted by trial and error indicated a very large dependency on initialisation time. Two domains have been used: one mother domain and one nest (figure 8). A 'perfect' run initialised at 28 October 00 UTC showed a core pressure, frontal structure and wind speed north of the Netherlands which almost perfectly matched real observations. However, a run initialised at 27 October 18 UTC did not let the wave develop until above Denmark and thus could be regarded as unrealistic. Moving nests have also been tested and did not provide a satisfying solution either. As such, the model has been reinitialised every six hours, in that way taking the development of the system into account. This method does not come at computational cost fortunately.

The outer domain ('Domain 1') has a resolution of 9 km and contains 200 x 180 grid cells It covers most parts of Western and North-Western Europe, as well as parts of the Northern Atlantic ocean where the storm originated. The inner domain ('Domain 2') has a horizontal resolution of 3 km and contains 241 x 241 grid cells. It covers a large part of the cloud head, including the region where sting jets occur in general and parts of the bent-back occlusion. This nest is moved manually every six hours (so for every new run) in order to be situated around the core of the low pressure system. Note that though this nest is being moved every six hours, this does not mean that the moving nest method has been used. The latter implies a different compilation of WRF.

For both domains, the vertical resolution consists of 70 levels, with level spacing increasing aloft. The lower boundary is located at the surface (excluding four soil layers present in the model runs) and the upper boundary at 50 hPa.

Table 1: Parameterizations used

Parameterization	Scheme
Cumulus physics	Kain-Fritsch (KF) cumulus scheme
Microphysics	WRF Single moment microphysics 6 (WSM6)
Short wave Radiation	Dudhia short wave
Long wave Radiation	Rapid Radiative Transfer Model (RRTM)
Boundary layer and surface layer	Mellor-Yamada-Nakanishi-Niino2 (MYNN2)
Surface layer option	Monin-Obukhov Similarity scheme
Surface physics	Noah Land-Surface Model
Urban physics	Urban canopy model

The following parametrisations were used and have not been altered during the experiment (table 1). The parametrisation schemes are the same as the ones used in (Browning 2015), as they already successfully modelled the St. Jude's Day storm using these settings.

3.2 Model experiments and data analysis

This subsection will be a walk-through of the research questions and subquestions.

The first research question was stated as follows:

How do the sting jet forming factors Conditional Symmetric Instability (CSI), evaporation and frontal dynamics in the sting jet region change during the development of a Shapiro-Keyser type extratropical cyclone?

The first subquestion was defined as follows:

1. *Which trajectories do air parcels follow before entering the sting jet region?*

   The assessment of this question has been done using the LAGRANTO lagrangian Analysis Tool (version 2.0, Sprenger & Wernli (2015)). To identify the sting jet region, the criteria as defined by L. H. Baker et al. (2014) have been used. These are: 1) The air originates at mid-levels within the cloud head, located between 600 and 800 hPa; 2) the air descents along a sloping surface of θ_w; 3) a reduction in RH during the descent; 4) strong winds and wind gusts at the top of the boundary layer.

   Cross-sections were made to determine where jets occur. These cross-sections include wind speed and relative humidity. Visual assessment was conducted on tbese cross-sections to identify whether a jet showed SJ behaviour.

   The location of the jet was compared to the theoretical SJ area (at the south-east side of the low-pressure centre). After the latter assessment, trajectory analysis was conducted with coordinates and height of the identified jets in LAGRANTO.

2. *Which areas on the south side of the low pressure centre show CSI?*

   In order to see whether CSI occurs or not, assessment of saturated moist potential vorticity (MPV*) has been conducted using the following sub-questions:

   - *Where do areas with negative MPV* occur?*
   - *What is the magnitude of MPV* in the sting jet region?*

   Areas of negative MPV* were identified and compared to the expected sting jet region. Furthermore, a comparison has been made with trajectories following the previous sub-question. Thereafter, the magnitude of MPV* was identified and compared to values from literature.

3. *How much evaporation is taking place in the sting jet region?*

   The total amount of evaporated water has been assessed by calculation with equation 3. The latter formula can be used to calculate the total amount of evaporated liquid water, using common WRF output variables such as temperature and air pressure. The calculated evaporation is the amount of phase-changed water when an air parcel is brought from aloft to lower altitudes, in this case from 700 to 850 hPa.

   It is assumed that an air parcel is constantly on a saturated level due to precipitation falling into the parcel. This assumption leads to a hypothetical maximum evaporation using the difference between $q_{sat,850}$ and $q_{sat,700}$.

   In most sting jets, evaporation is probably smaller than this value as precipitation does not always occur. This would therefore require the use of liquid water content q_{liquid}, which is used to increase q_{sat} when descending, until all q_{liquid} has been evaporated. The latter uses the assumption of constant conditions in the air parcel (e.g. no precipitation, no water molecules being transported into the parcel). As we wanted to know the maximum possible evaporation in ideal conditions, the latter method has not been used. The truth probably lies somewhere in the middle between this maximum and minimum evaporation.

4. *How much frontolysis is taking place in the sting jet region*

   - *How large is the time rate of change of the magnitude of the horizontal gradient of potential temperature (i.e. Pettersen Frontogenesis) at the end of the back-bent front?*

   The Petterssen Frontogenesis factor was plotted by using equation 10. The necessary fields for this equation are already present as output values in WRF and were combined.

What is the interaction of Conditional Symmetric Instability (CSI), evaporation and frontal dynamics in the sting jet region?

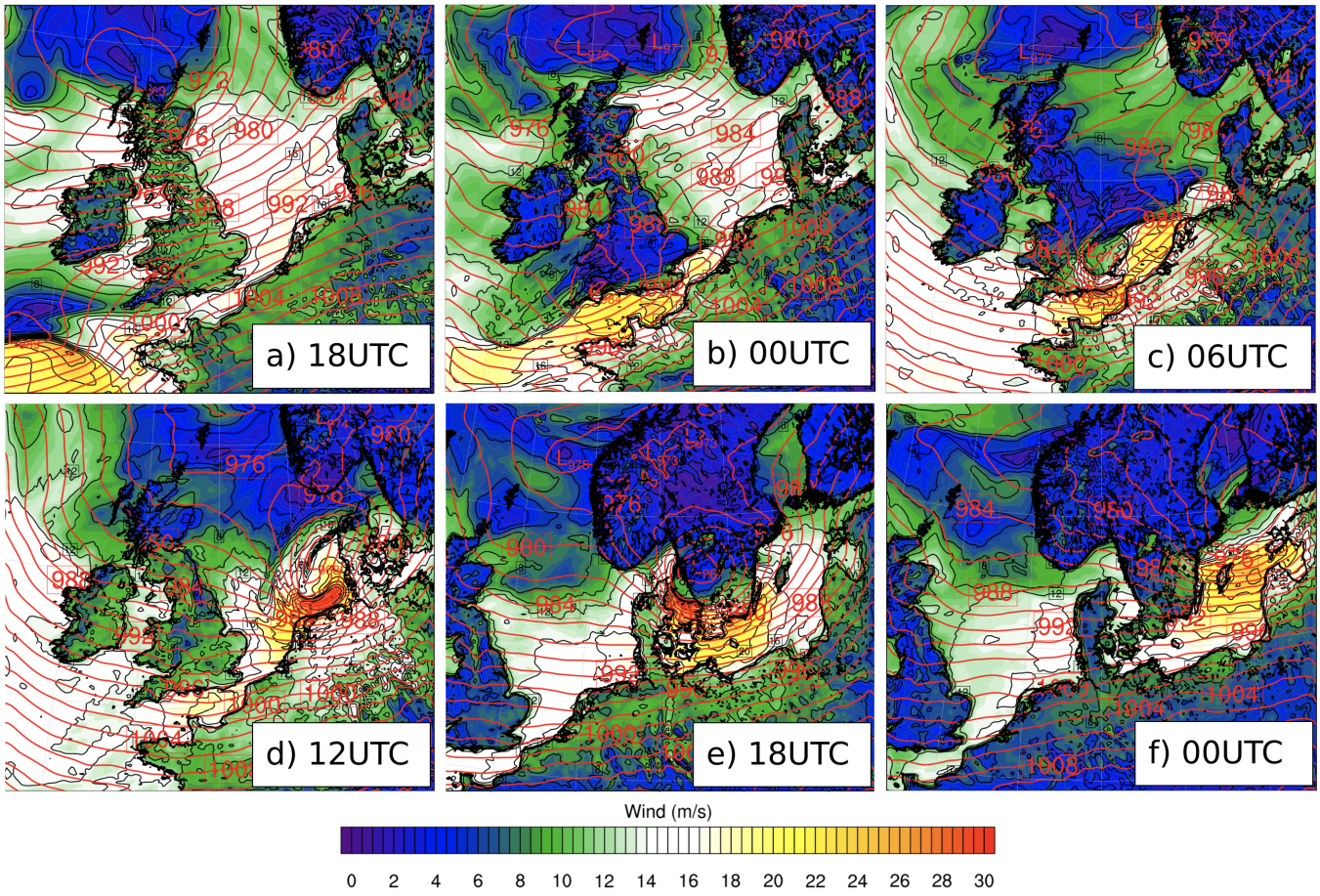

Figure 9: Modelled wind speed (colours and black contours) and sea level pressure (red contours). A wave disturbance is located at the lower left of figure a. It develops rapidly and reaches a minimum pressure at 12 UTC (d). Wind speeds of more than 30 m/s are reached.

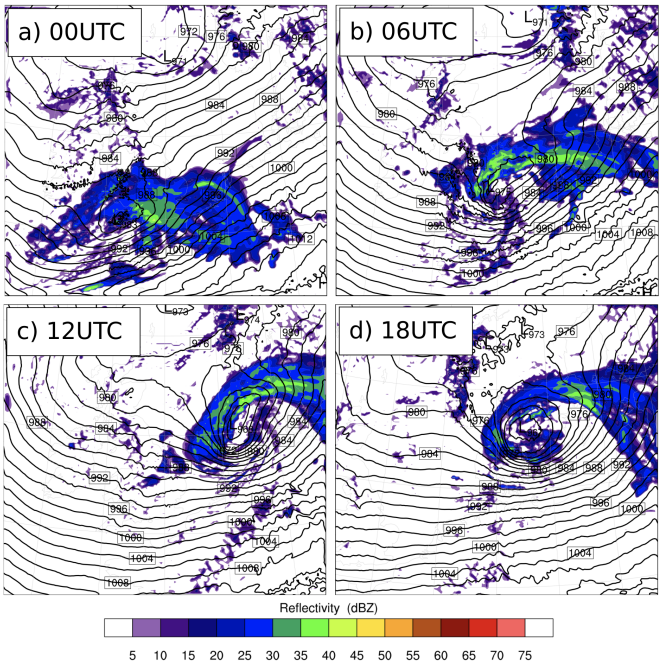

Figure 11: Modelled precipitation (colours) and sea level pressure (contours). The most active precipitation area is located at the northern side of the core. The cold front is inactive, showing only minor showers. The front is fractured and has a T-bone shape.

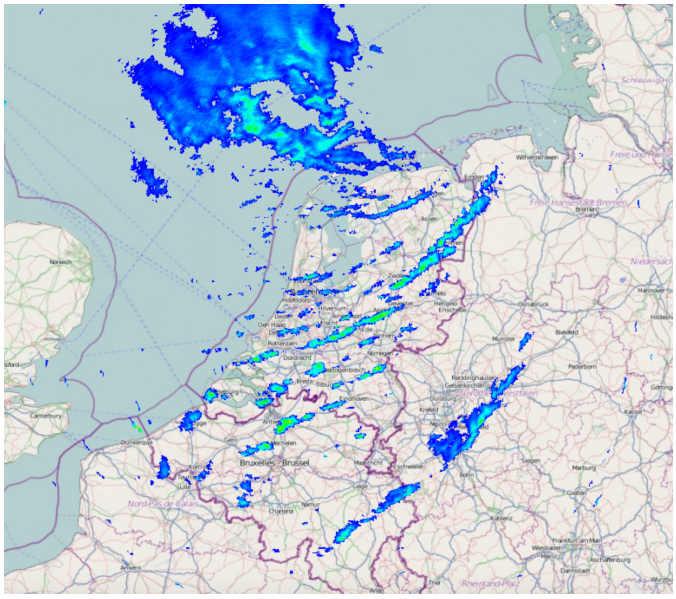

Figure 12: Precipitation as observed by the KNMI radar. Aligned showers are visible above The Netherlands. A part of the bent-back occluded front is located above and north of the Wadden islands as a stratiform area of rain. (KNMI ADAGUC)

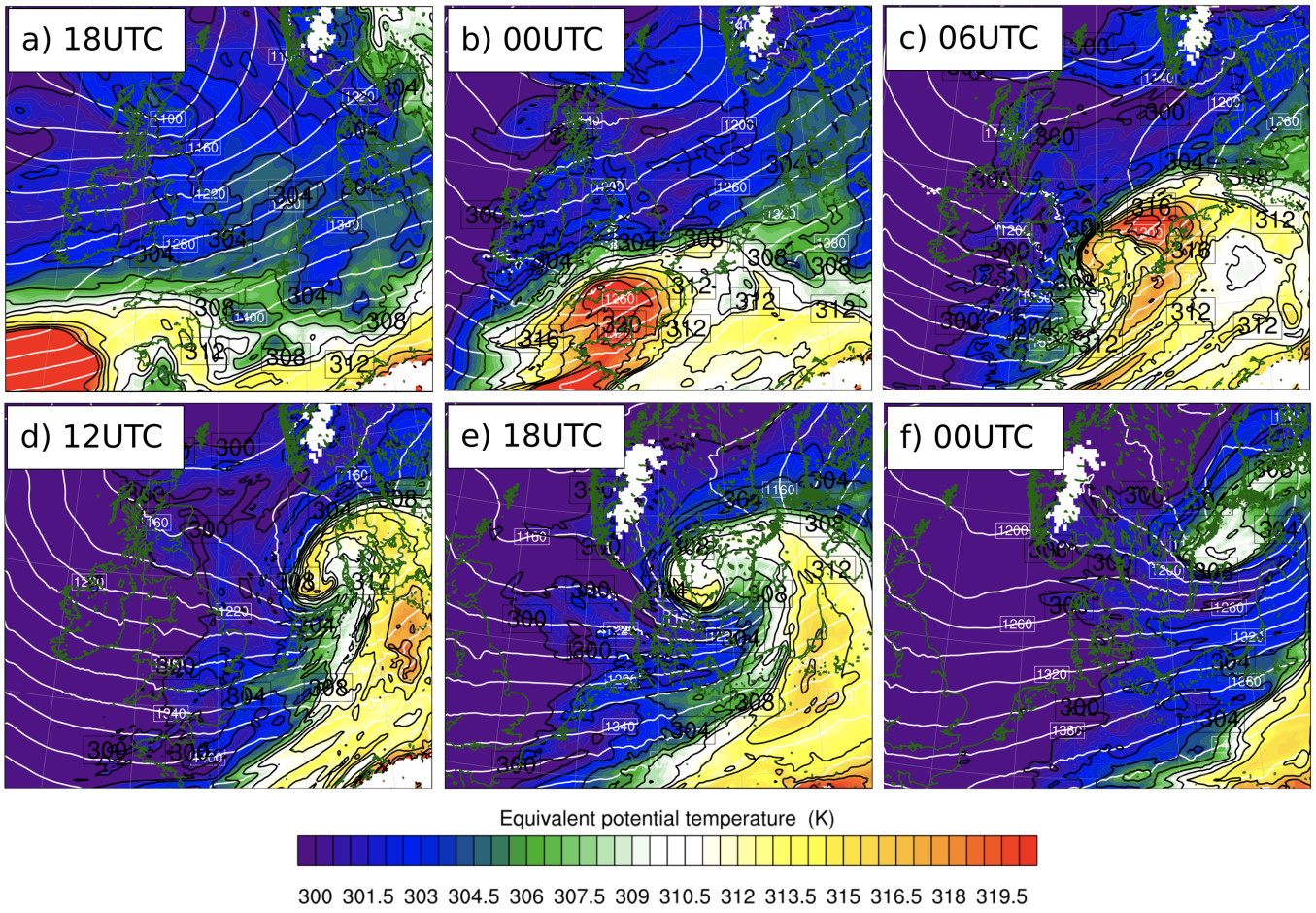

Figure 10: Modelled equivalent potential temperature (colours and black contours) and geopotential height (white contours). Redder colours indicate warmer temperatures. An area of warm air is advected over Western-Europe. A clear warm sector develops and equivalent potential temperature gradually decreases as the storm progresses. Clear frontal structures can be seen at large gradients of θ_e. The left gradient is the from low to high θ_e is the cold front. The north-eastern gradient in figure c is the warm front and an occluded front wraps around the low pressure centre (edge of the curl). In figure e, an area of warm air is secluded into the core.

The last research question assessed the interaction between all important sting jet factors. It summarizes and provides a comparison between all output created before. Visual assessment of earlier produced figures and values has been conducted to get insight in which process influences another and what the order of processes is for each time step.

4 Results

4.1 Low-pressure development: model compared to observations

4.1.1 Pressure and precipitation

Model output shows a rapidly deepening low pressure system (figure 9). On 27 October, 20 UTC, a core pressure of 988 hPa is reached. This is also the first time the model shows closed isobars and thus a clear low pressure area. The location and depth of the low pressure core compare well to observed values of sea level pressure (figure 1).

8 hours later, on 28 October at 06 UTC, the depression has deepened to 975 hPa. As such, the average pressure fall during this time period is 1.6 hPa/h. At 12 UTC, the model sea level pressure reaches 968 hPa. The latter compares very well with observed values of 967 hPa, as these values are within 1 hPa from each other. Moreover, the modelled and observed core locations are within a range of 50 km and timing seems to be accurate to the hour. The shape of the area of low pressure at 12 UTC is elongated, which creates a sharp bending point of the isobars at the southern edge of te core.

At 13 UTC, an area of warm air is cut of in the core (warm core seclusion) (figure 10). At this stage, the extratropical cyclone does not deepen further. The minimum pressure is reached and amounts 966 hPa approximately. After 17 UTC, the pressure starts to rise again (figure 9). During this time period, the shape of the pressure

field changes from elongated to circular. On its path over southern Scandinavia, pressure rises slowly and the storm tends to weaken. The latter is in accordance with observations.

An extensive area of precipitation is associated to the initial wave. During its development, most precipitation is located on the northern and western side of the core (figure 11). From figure 10, it can be derived that this large band of precipitation collocates with the occluded front. When looking at the cold front, however, precipitation seems to be almost absent. Only light showers occur in the latter region. On the south side of the low pressure centre, the model produces lines of light showers which are parallelly curved with respect to the bent-back occluded front.

Comparing the modelled areas of precipitation to radar observations, large similarities can be seen (figure 12). In both observations and model, most precipitation is located near the occluded front. The cold front shows only light showers and also showers on the south side of the low pressure core can be discerned from the model as well as radar observations.

4.1.2 Wind speed and gusts

Strongest winds were observed on the south side of the low pressure system. As the wave develops, wind speed and gusts increase and a narrow area of highest velocities starts to develop. In general, wind speeds of 20 - 25 m/s are modelled over the English Channel (figure 9). At 06 UTC, winds reach almost 30 m/s in a very small area just south of Brighton. Wind gusts reach 145 km/h (figure 13). Observations do not show these excessively high wind speeds in a small area. However, the general picture seems to be correct.

Highest wind velocities and gusts are modelled between 09 UTC and 13 UTC. Wind speed south-east of the bending point of the isobars is in excess of 30 m/s and wind gusts are higher than 150 km/h. This is in accordance with

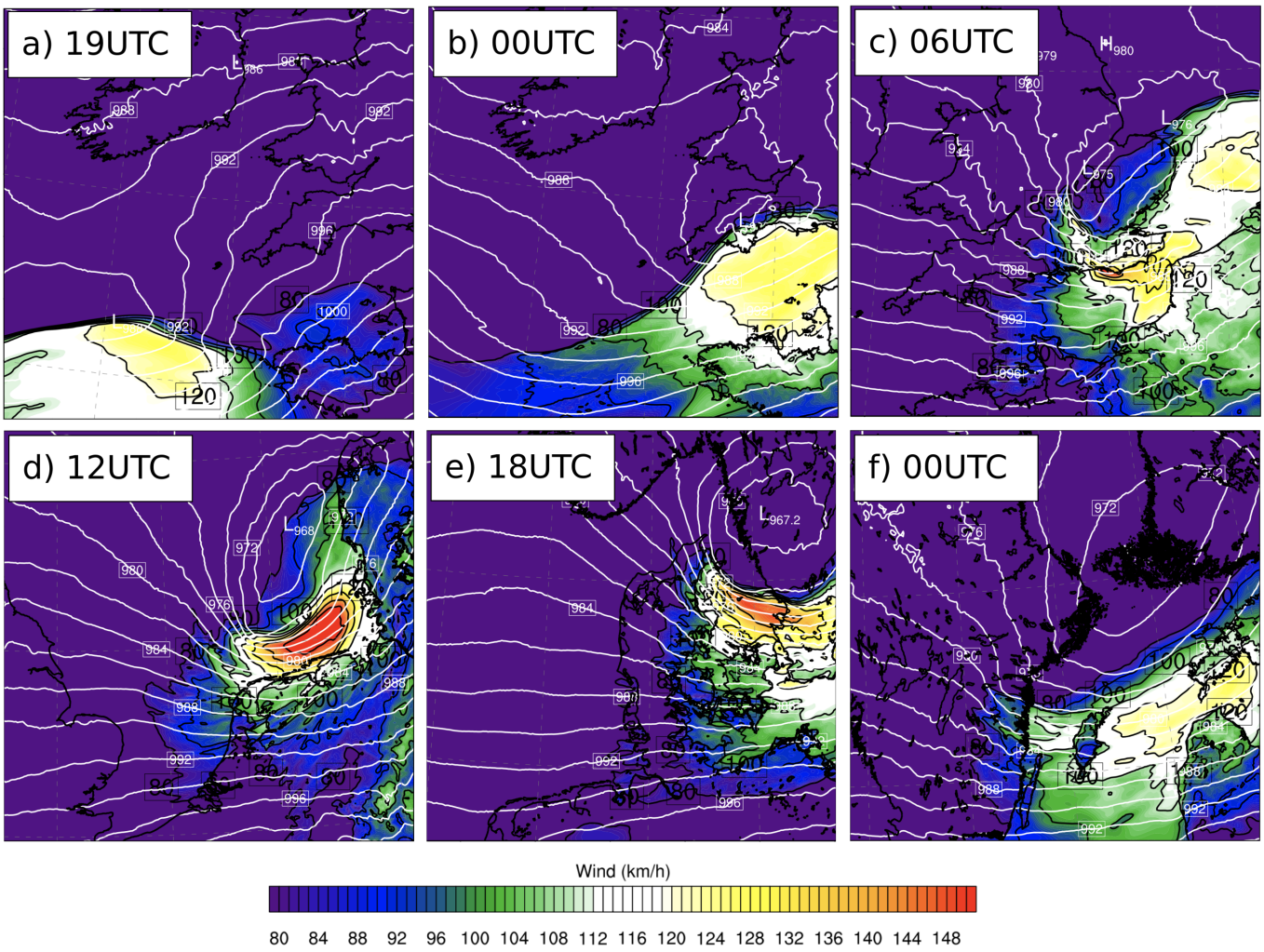

Figure 13: Modelled wind gusts (colours and black contours) and sea level pressure (white contours). strong wind gusts are visible in the warm sector during the wave-phase (figure a, b, c). An area with maximum gusts develops south of the coast of England (figure c). Maximum gusts are reached around 12 UTC (figure d) and amount more than 150 km/h.

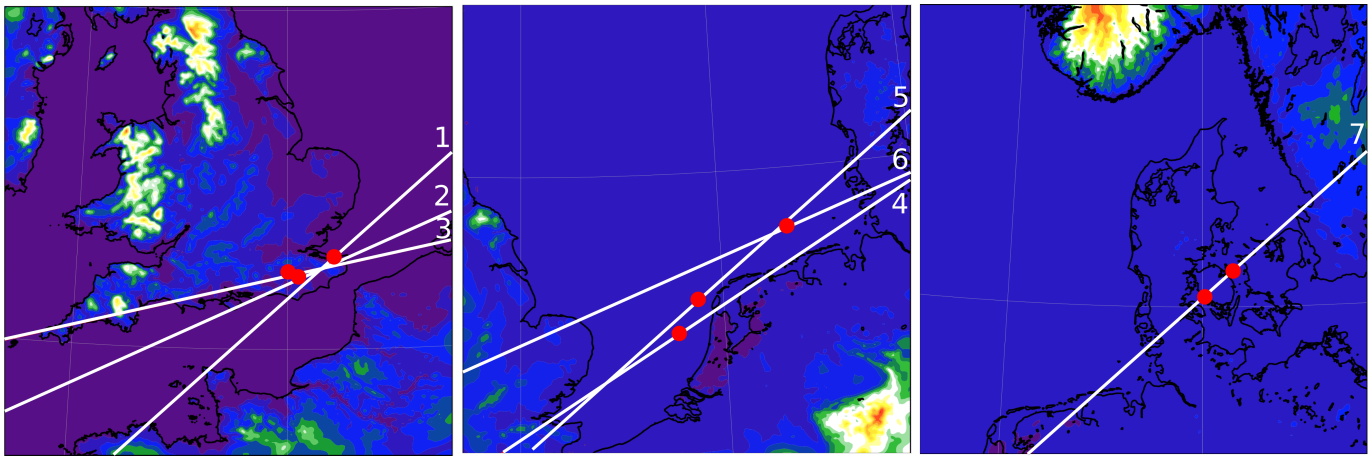

Figure 14: Map of cross-sections in three different domains. Cross-sections are numbered 1-7. Red dots indicate the location of sting jets in these cross-sections.

observations. On the north coast of the Netherlands and on the Wadden Islands, gusts of 154 km/h were measured. Moreover, 10-minute averaged wind velocities of approximately 120 km/h were measured, which is equal to 12 Bft. The location of the narrow band of strongest winds is almost spot on compared to observations. Furthermore, timing seems to be perfect. The model seems to let both wind speed and gusts decrease on its path over northern Germany and Denmark. This is slightly off, since gusts over 170 km/h in Germany and even 193 km/h in Denmark were observed. Note that all mentioned gusts were measured in areas without much relief, thus without hills or mountains. Besides the band of strongest wind gusts, other areas of high velocities can be discerned (figure 13). These feature a linear shape and occur over land as well as over sea. These gusts are, however, not as strong as in the area south-east of the core, reaching approximately 110 km/h. They seem to be associated with linear bands of showers (figure 12 and 11).

4.2 Sting jet

4.2.1 Development

From theory, sting jets occur in stage two and three of a Shapiro-Keyser cyclone and are located south-east of the low pressure core. To determine whether SJs occurred, cross-sections were made (figure 14), after which trajectory analysis was conducted on possible sting jets.

At 06 UTC, three cross-sections were made. Cross-section 1 (CS1) runs from Brittany to the North-Sea, through Cherbourg and Kent (figure 14). Cross-section 2 (CS2) is more or less parallel to the coast of Southern England and crosses Kent (figure 14). Cross-section 3 (CS3) is located over the southern coast of England and runs from Kent to Cornwall.

In all cross-sections, several distinct jets can be discerned (figure 15). For all jets, trajectory analysis revealed the origin of air parcels.

CS1 contains one jet which shows sting jet behaviour. This jet is located between 1200 and 2200 m above the surface and occurs just north-east of Kent. Within the cross-section through the SJ, a gradient of relative humidity is present. RH rises from approximately 30 % at 2200 m to almost 100 % at 1200 m.

Within the SJ trajectory (not shown), RH drops from 57 % at 00 UTC to 21 % at 05 UTC. RH rises slightly to 28 % at 06 UTC. Between 00 UTC and 06 UTC, the air parcel descends from 3300 m to 2000 m. Wind speed increases from 35 m/s at 00 UTC to 45 m/s at 06 UTC. Due to the relatively low starting point of RH and increasing RH vertically when coming from aloft, this jet might not be a SJ. However, the stark descent and increase in wind speed make it plausible.

The other jet in CS1 does not show SJ behaviour. The jet is located between the surface and approximately 800 m, which would be relatively low in the case of a SJ. Within the trajectory, RH fluctuates between 100 % and 90 % approximately. Wind speed increases from 4 m/s at 00 UTC to 41 m/s at 06 UTC. The air parcel ascends from 213 m to 500 m. Since descent is absent, wind speed increases rapidly and RH is fairly high, this jet is probably the cold conveyor belt jet (CJ). The CJ runs along the bent-back occluded front and reaches its maximum just east of the bending points of the isobars.

In CS2, one sting jet can be discerned (figure 15). The SJ is located on a horizontal gradient of RH (approximately 100 % west of the jet to 60 % east of the SJ). The jet has a maximum wind speed of approximately 44 m/s. The sting jet emerges at 04 UTC and starts at an altitude of approximately 2400 m (figure 18). Between 00 UTC and 04 UTC, the air parcel of the trajectory analysis rises from 2100 m to 2400 m. During these six hours, the air accelerates from 17 m/s to 44 m/s. When descending, RH humidity drops from 100 % to 59 %.

The lowest jet was determined to be a CJ, since air originated from altitudes between 900 and 1500 m. Furthermore, RH remains high during the air parcel's movement. On average, RH values 94 %, with peaks of 100 % and

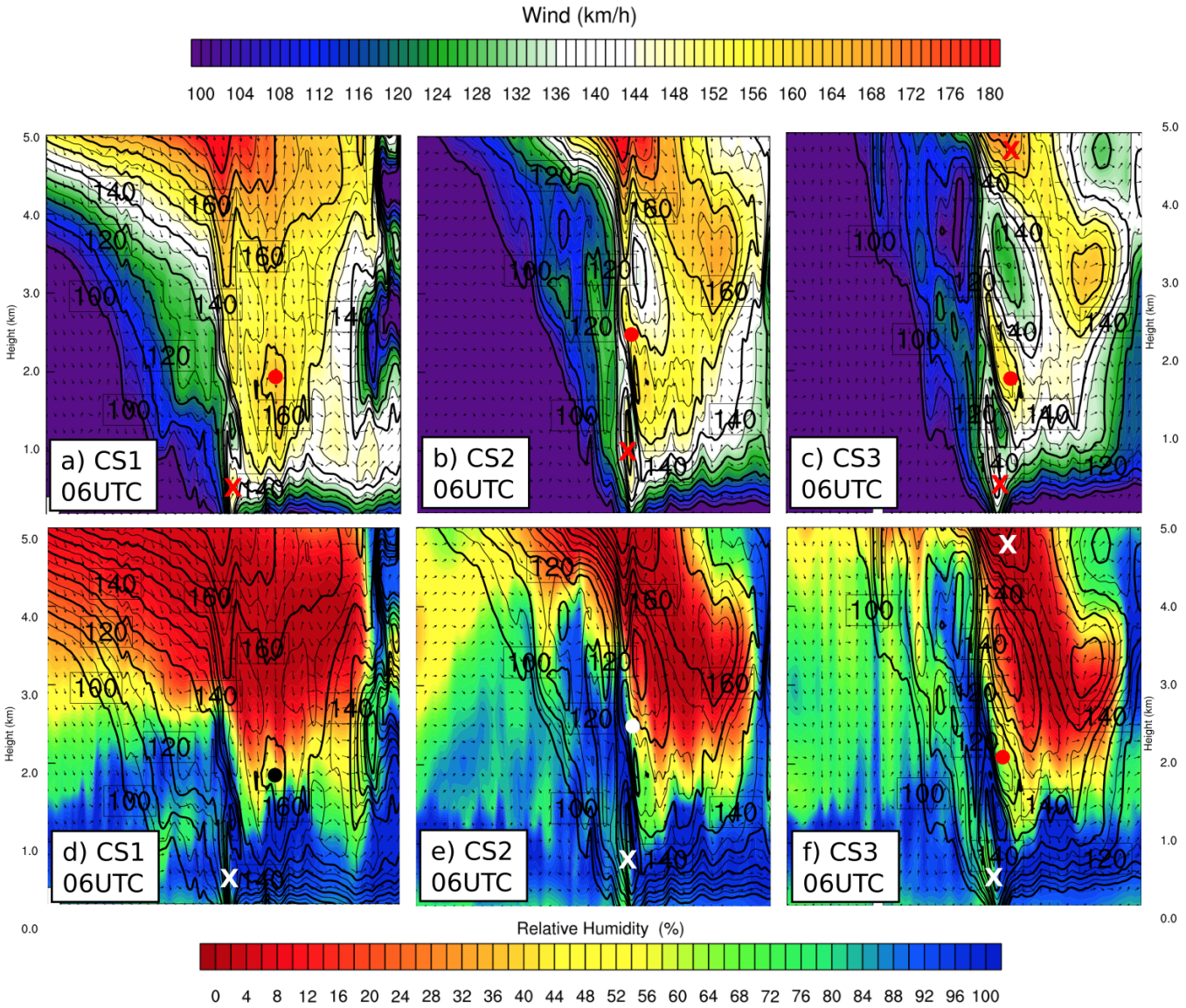

Figure 15: Cross-sections at 06 UTC. Figures a, b and c are cross-sections of model wind speed (colours and contours), figure d, e and f of model RH (colours are RH, contours are wind speed). Figures are vertically aligned to make comparison between similar cross-sections of RH and wind speed easier. Dots indicate sting jets, crosses indicate CJs and DAs (cold conveyor belt jets and dry air streams). Different colours are used in order to improve visibility of dots and crosses to the background colour and do not have any meaning to jet properties.

a minimum of 81 %. Trajectory analysis revealed strong acceleration, from approximately 4 m/s at 00UTC to 44 m/s at 06 UTC.

In CS3, three jets are modelled above each other vertically, located around the Greenwich meridian (figure 15). A revolving pattern is visible: there is a lower jet at 1 km (CJ), a middle jet at 2 km (SJ) and a top jet at 5 km (Dry Air stream, DA). The jets are separated with areas of relatively low wind speed. In this cross-section, the jets slope downwards in the eastern direction (i.e. to the right in figure 15).

Trajectories of the SJ in CS3 show similar characteristics as CS2: RH and wind speed decrease and increase with the same order of magnitude. This is due to the fact that both trajectories belong to the same SJ, captured in two different cross-sections.

Analogous to the previous analyses of jets in cross-sections, sting jets have been found at 09, 10 and 12 UTC (figure 16). In CS4, a SJ is located at 1500 m, in the centre part of the southern North-Sea. The air parcel descends from approximately 2500 m to 2100 m. The descent starts at 06 UTC. Before this time, the air parcel ascends from altitudes below 2000 m to 2500 m. During the air parcel's course, acceleration from 7 to 39 m/s occurs. Furthermore, RH drops from 95 % to 55 %.

CS5 shows two distinct jets at 10 UTC, of which one is a SJ and the other is the CJ. The SJ is located at 2000 m approximately, whereas the CJ has an altitude of 500-1000

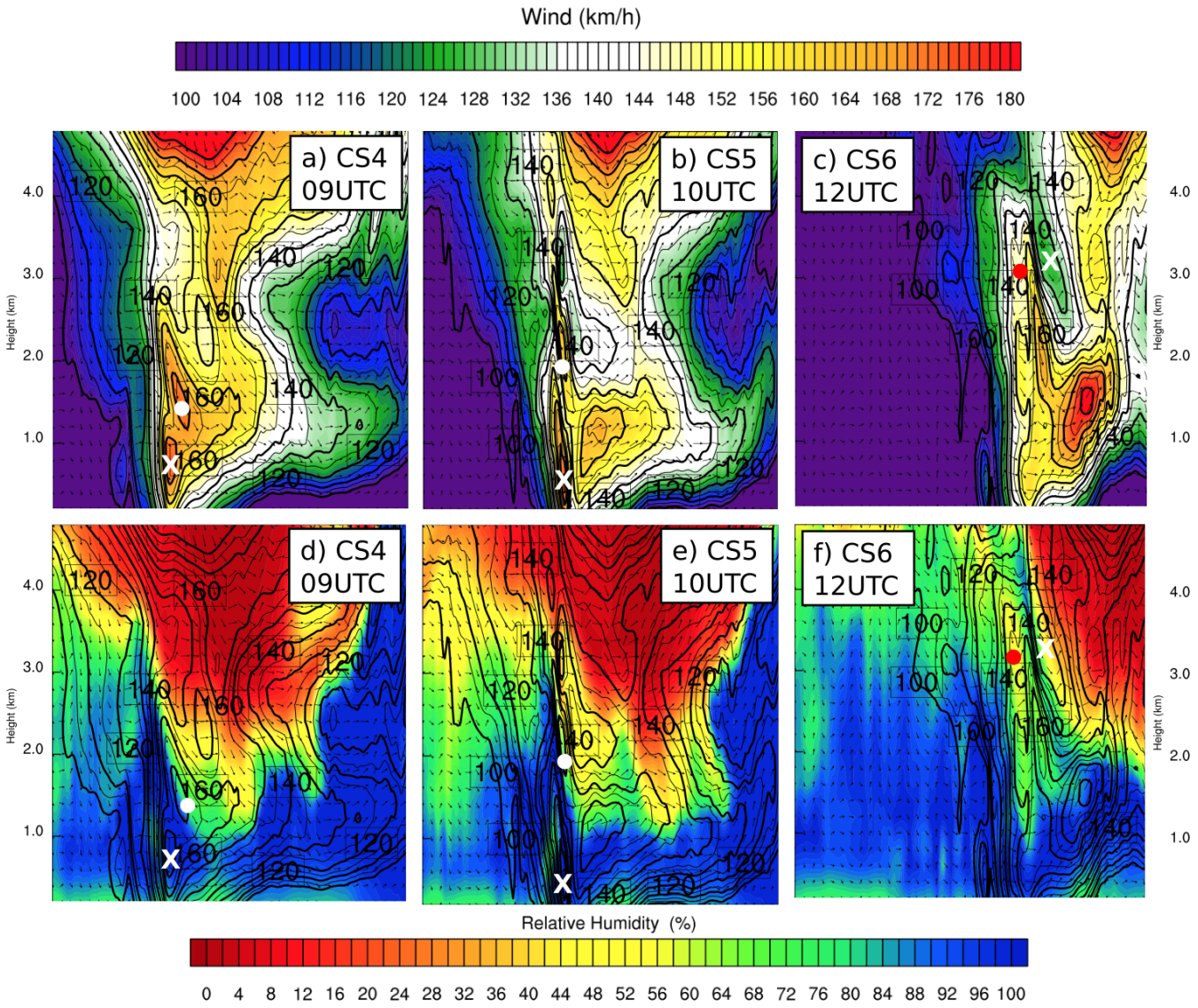

Figure 16: Cross-sections at 09, 10 and 12 UTC. Figures a, b and c are cross-sections of model wind speed (colours and contours), figure d, e and f of model RH (colours are RH, contours are wind speed). Figures are vertically aligned to make comparison between similar cross-sections of RH and wind speed easier. Dots indicate sting jets, crosses indicate CJs and DAs (cold conveyor belt jets and dry air streams). Different colours are used in order to improve visibility of dots and crosses to the background colour and do not have any meaning to jet properties.

m. Trajectory analysis reveals a descent of 300 m in the last 2 hours. During descent, RH drops from 95 % to 60 % and wind speed increases from 17 m/s to 46 m/s.

In CS6 at 12 UTC, one sting jets is situated between 3500 m and 2500 m, west of an area of remarkably lower wind speed (figure 16). RH is low compared to the environment, with values of 50 % against 70 %. The SJ originated at 10 UTC and thus is relatively young. Trajectory analysis shows ascent from approximately 1600 m to altitudes above 3000 m (depending on the trajectory).

In the last hours, the air parcel descends a few hundred metres. During descent, RH drops from values near 100 % to almost 50 %. This is a rather large drop in relative humidity when taking the small change in altitude into account.

From 00 UTC to 12 UTC, the air parcel accelerates from approximately 10 m/s to 40 m/s. Some trajectories show constant acceleration, others show a mixed pattern with deceleration occurring as well. In general, during the descending branch of the air parcels (between 10 and 12 UTC), wind speed increases from 30 to 40 m/s.

Moving forward in time, during the declining phase of the St. Jude's Day storm, CS7 was made (figure 17). This cross-section runs from the Flevoland province in the Netherlands, over Northern Germany, the large Danish islands and Southern Sweden.

At 15 UTC, two jets show sting jet behaviour. In a timespan of 13 to 15 UTC, air descends from approximately

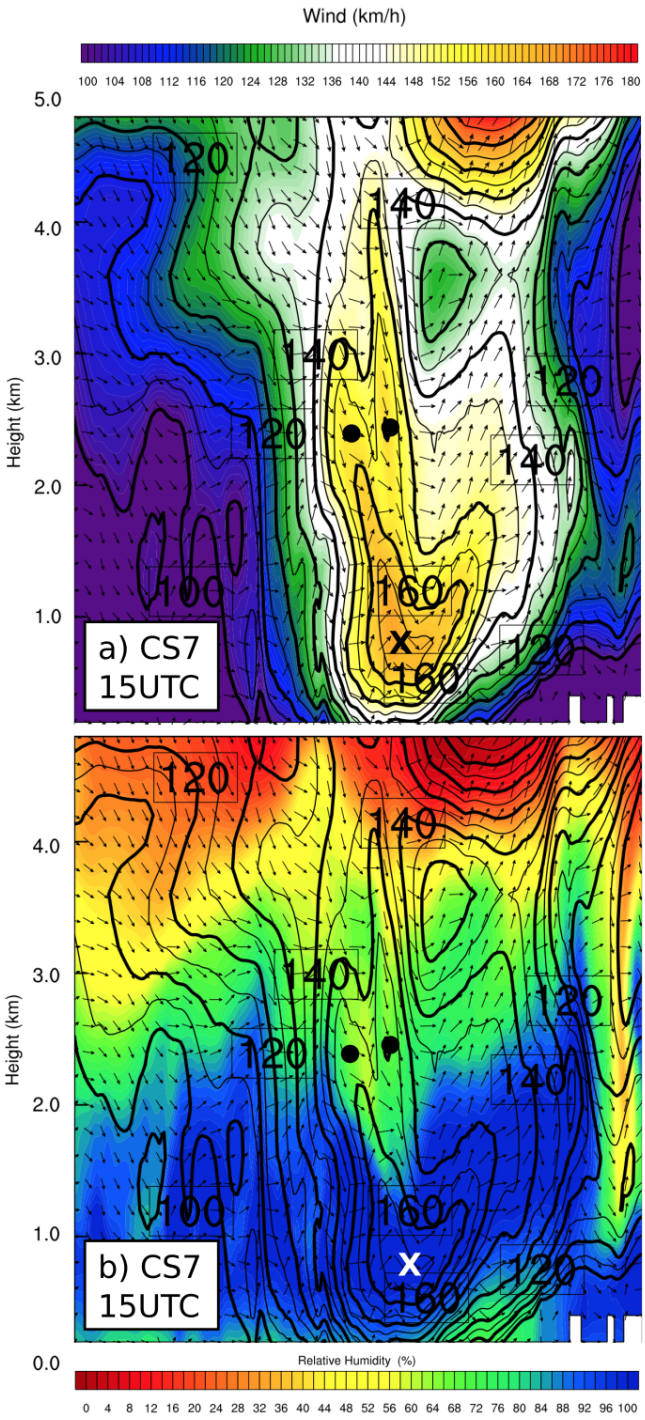

Figure 17: CS at 15 UTC. Figure a is model wind speed (colours and contours) and figure b model RH for the same cross-section (colours indicate RH, contours wind). Dots are identified sting jets, the crosses indicate a CJ.

2800 m to 2500 m (figure 18). The air in both air parcels shows lower values of RH at 15 UTC. RH drops from 92 % to 60 %. Wind speed increases from approximately 20 to 45 m/s accordingly.

The drop in RH is large enough to compensate the RH from downward motions alone. However, the difference in altitude is only 300 m, which is on the lower side of SJ behaviour. Furthermore, RH increases from almost 40 % to more than 90 % before 13 UTC. This would not comply with sting jet theory. As this large increase in RH occurs at time of reinitialisation, a possible explanation would be a displacement in weather systems created by different model times. As such, these jets possibly are sting jets, but there is some uncertainty.

The lower jet in figure 17 is not a sting jet. The jet altitude is very low (only 1000 m above the surface) and RH is almost constantly 100 % during the air parcel's movement. As such, this jet is probably related to the cold conveyor belt. After 15 UTC, no sting jets have been observed from model data.

4.2.2 Evaporation

Evaporation was defined using equation 3 and as such displays the difference in water content due to phase changes between two layer representative for a SJ. This is not exactly evaporation from a theoretical point of view, but we will use the term 'evaporation' for this process as a simplification.

During the rapid development in the pro-wave phase (between 00 and 06 UTC), evaporation increases from approximately 2 g/kg to 8 g/kg (figure 19). The most notable changes occur at 02 UTC when a small but distinct area of larger evaporation emerges south of Devon. Furthermore, a gradual increase of another evaporative area occurs from 03 UTC onwards, after which both combine at 05 UTC. The area of strongest evaporation coincides with the sting jet region during this phase of the extratropical cyclone.

When moving north-eastwards, the area of strong evaporation seems to attach itself to the core of the low pressure area and has developed a full cyclonic pattern at 11 UTC. After this time, the amount of evaporation declines to 4-6 g/kg in general. Highest values are found on the eastern edge of the core. Slightly lower values are found south-east of the system near the cold front. When moving forward in time, the latter area moves further away from the low pressure centre. At 29 October 00 UTC, evaporation is weak and in the order of 2-4 g/kg, which is slightly higher than 0-2 g/kg which can be found elsewhere in figure 19.

Note that the area of strongest evaporation moves further away from the core when the cyclone progresses. The consequence of the latter is that strong evaporation does not coincide with the sting jet region any more. This change starts approximately at 09 UTC.

4.2.3 Conditional Symmetric Instability

Conditional Symmetric Instability (CSI) has been determined with saturated moist potential vorticity (MPV*). When MPV* is negative, CSI can be released.

At 00 UTC, positive values of MPV* can be found on a trough or cold frontal axis of the developing wave (where the geopotential lines in figure 20 bend southward). This

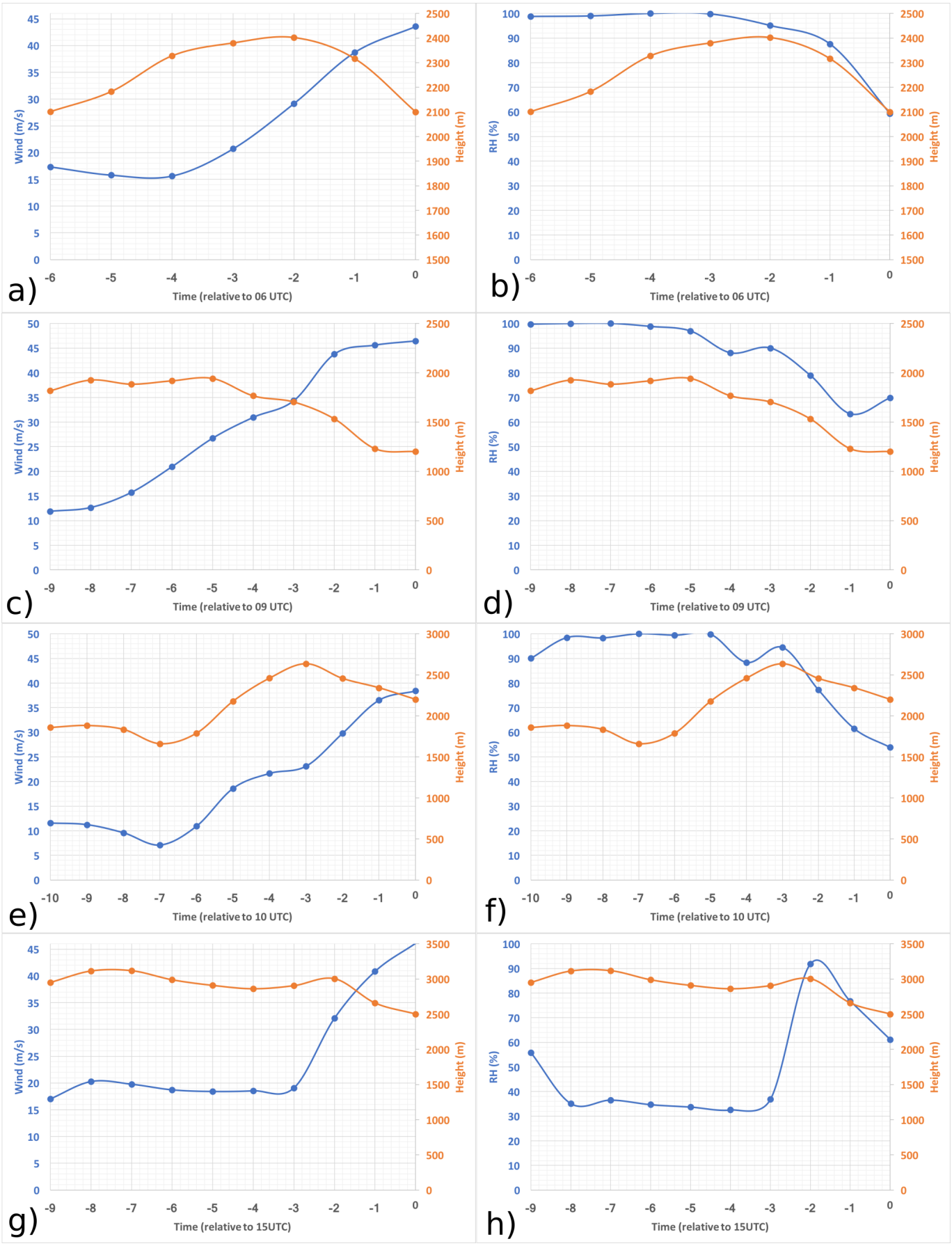

Figure 18: Trajectory time series of SJ air parcels. The orange lines indicate air parcel heights and the blue lines wind speed and RH respectively. All figures on a row (a and b; c and d, etc.) form pairs. Time (horizontal axis) is relative to the starting point of the trajectory analysis, i.e. a and b start at 06 UTC, c and d at 09 UTC, etc. Note that in figure a and b the height axis starts at 1500 m instead of at the surface. This has been done to create a better visualisation of the small descent of the air parcel.

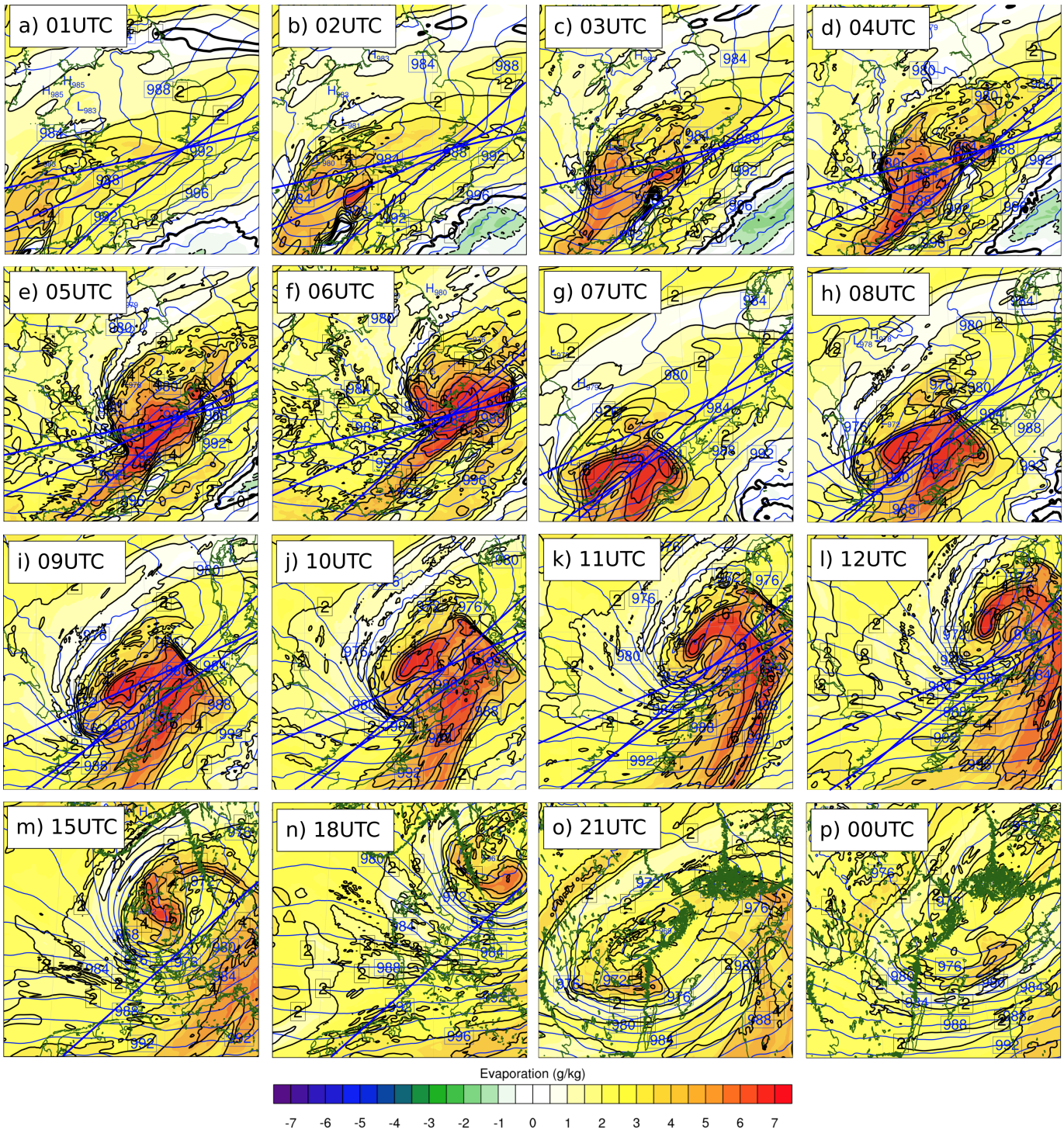

Figure 19: Calculated evaporation from model results (colours and black contours) and model sea level pressure (blue contours). The blue lines indicate cross-sections of figure 15, 16 and 17. An area of strong evaporation (more than 6 g/kg) develops south of the coast of England (figure b). The latter area extends during the storm's progression and develops a shape similar to the extratropical cyclone. The amount of evaporation decreases after 12 UTC. Note that 1-hourly steps are used for figure a-l and 3-hourly steps from figure m-p. Furthermore, as the inner domains are shifted every six hours, a displacement of features is visible between the figures.

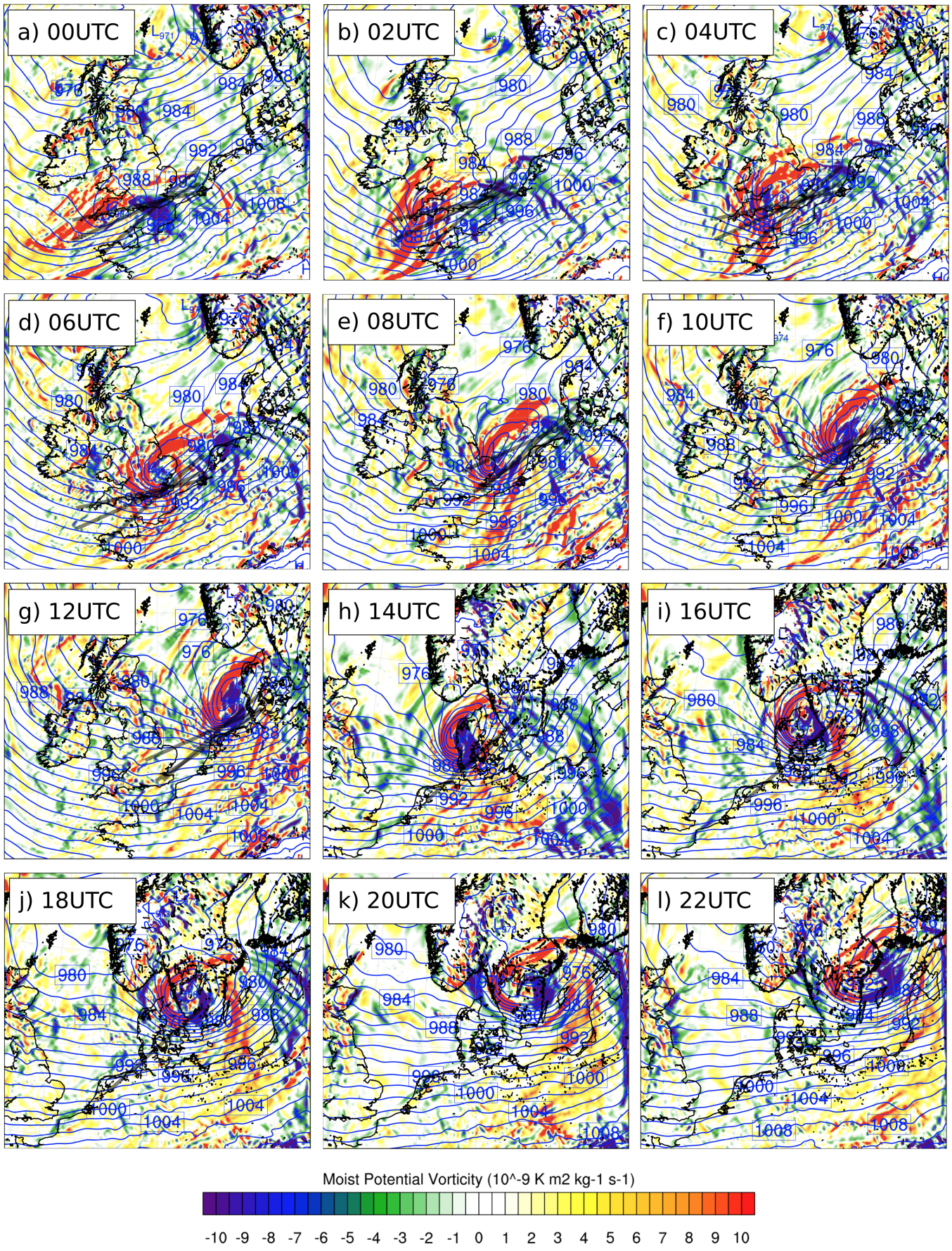

Figure 20: calculated saturated Moist Potential Vorticity from model results at 850 hPa (colours) and model sea level pressure (blue contours). The black lines with lower opacity indicate cross-sections of figure 15, 16 and 17. An area of CSI develops at the south-eastern flank of the low pressure core and increases in size. The latter area collocates with the SJ region from 04 UTC approximately.

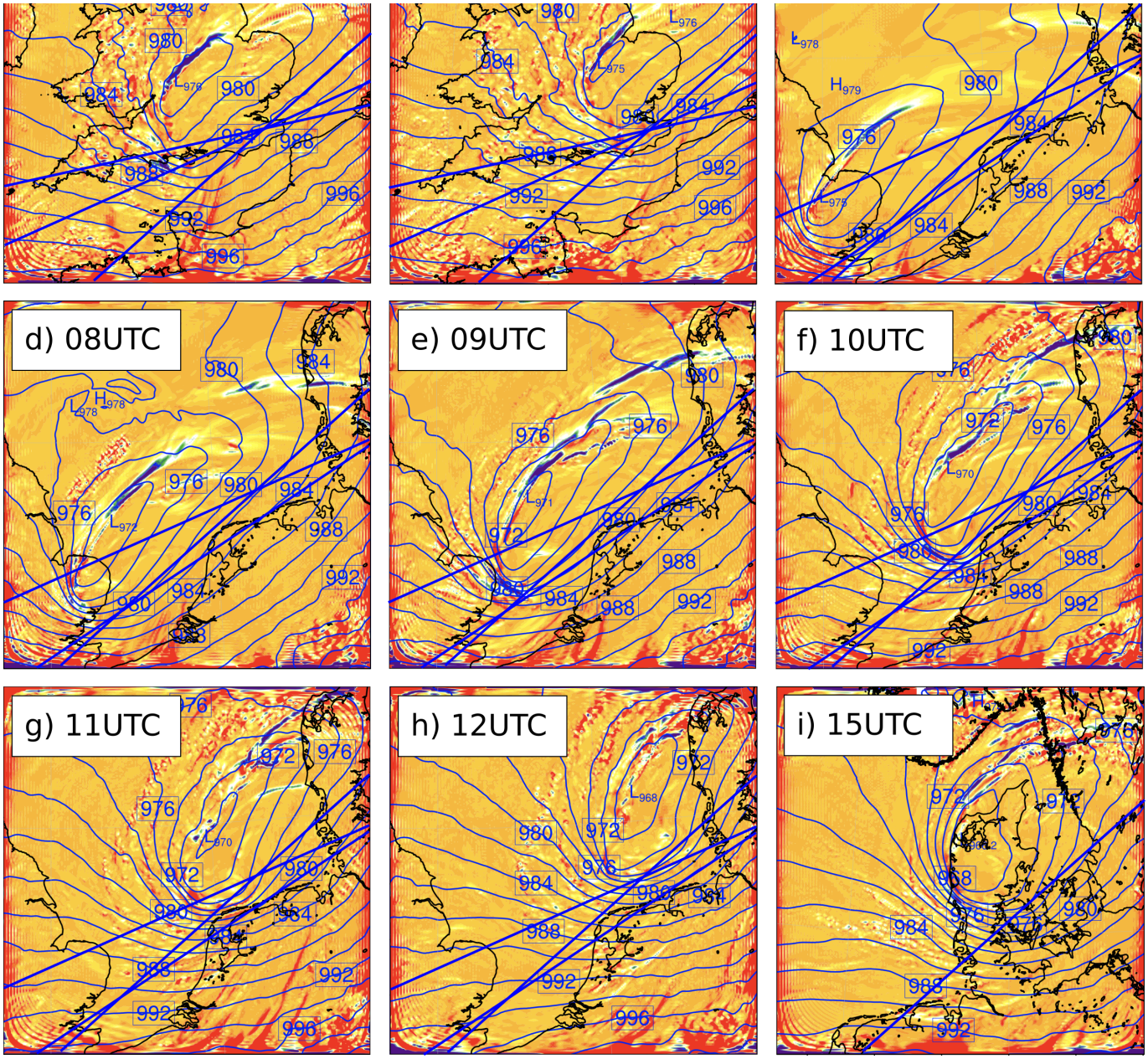

Figure 21: Calculated Petterssen frontogenesis from model results at 850 hPa (colours) and model sea level pressure (blue contours). The blue lines indicate cross-sections of figure 15, 16 and 17. Frontolysis is denoted with blue colours and thus negative values of F. Only at 09 and 10 UTC, frontolysis collocates with the SJ region. Note the ripple effect at the boundaries. Furthermore, time steps of one hour are used in figure a-h and i is displayed three hours later.

vast area extends from northern Cornwall to at least western Brittany and is located above the Atlantic Ocean. Areas of negative MPV* and possible regions of CSI are located on the warm frontal axis over southern England and a region of similar size over Brittany. No CSI occurs inside the SJ region. The regions of negative MPV* show lower magnitudes compared to positive MPV* (-8 to -10 $Km^2kg^{-1}s^{-1}$ and more than 10E-9 $Km^2kg^{-1}s^{-1}$ respectively). From now on, we will only refer to negative or positive values of MPV* and whether their magnitudes have increased.

From 04 UTC onwards, an area of negative MPV* starts to develop in the SJ region over southern England. At 06 UTC, a small but distinct area of CSI can be found over Kent. Its values have approximately the same magnitude as the areas of positive MPV*.

At 08 UTC, two areas of negative MPV* start to merge, increasing the size of the area where CSI is possible. At 11 UTC, a fully developed couplet of negative MPV* at the south-eastern side of the low pressure core and positive values west and north-west of the core has emerged. The area of CSI coincides with the sting jet region and the end of the bent-back occluded front. The area of positive CSI coincides with the frontogenetic area of the bent-back occlusion.

As the cyclone progresses over Denmark and reaches a phase where the pressure deepening stops, the MPV* couplet starts to lose its shape. A distinct area of negative MPV* can be discerned on the south-eastern side of the core (figure 20). An area of positive MPV* wraps (along with the bent-back occluded front) around the low pressure centre. Inside the core, an area of fluctuating values of MPV* emerges.

During the last phase of the extratropical cyclone, in which the depression starts to decrease in strength, the clear pattern of negative MPV* at the end of the cloud head and positive values inside the bent-back occluded front gradually weakens. At 00 UTC, when the windstorm is located between Sweden and Finland, the latter pattern is diffuse. However, negative values of MPV* (and thus the possibility of CSI) are still in the SJ region.

4.2.4 Frontolysis and frontogenesis

The influence of frontolysis was determined using the Petterssen frontogenesis factor, which is defined as the change of temperature over a certain distance during a certain time period. Negative values of Petterssen frontogenesis indicate a decrease in the temperature gradient in the horizontal and as such frontolysis.

The signal of frontogenesis and frontolysis derived from modelled data of the St. Jude's Day storm (figure 21) is not very clear. Most areas show frontogenesis values of approximately 0.0 K/100km/day. This is in accordance with theory as fronts are linear and not very wide features.

However, frontolytic areas (negative values of F in figure 21) show up at the north side of the bent-back occluded front. This would imply that the front is decreasing in strength, whereas the extratropical cyclone is strengthening. In the SJ region, values of F fluctuate around 0.0 K/100km/day, indicating neither frontogenesis nor frontolysis are present at the end of the bent-back occluded front.

A small frontolytic signal is visible on the south side of the pressure core at 05 UTC, though disappearing at 06 UTC. The latter feature reappears at 09 and 10 UTC near or inside the SJ region, however, disappearing again at 11 UTC. The frontolytic area in the SJ region is bounded by frontogenetic features at its southern and northern boundary. A mixture of frontogenesis and frontolysis is still present at the occluded front (areas of negative and positive F are closely following each other).

After 12 UTC, the signal of F gets rather weak with no large frontogenetic or frontolytic areas. Only small spots of positive and negative values of Petterssen frontogenesis can be discerned. Note that white colours in figure 21 are not 0.0 but -0.4 K/100km/day. This has been done in order to give areas of frontolysis better visibility.

5 Disscussion

5.1 Gradient of RH

Several sting jets have been discerned from modelled data of the St. Jude's Day storm of 28 October 2013. These SJs occurred in the stage of strongest development of the extratropical cyclone and slowly disappeared after 12 UTC, when deepening of the core pressure stopped. Most sting jets were located between 2000 and 3000 m, situated near a strong horizontal gradient of RH. The latter is an interesting feature, as it could make SJ identification easier.

An explanation for the occurrence of SJs at a horizontal gradient of RH could be the evaporating nature of a SJ. This would imply that the air dries out strongly during descent and due to the skewed nature of a SJ, driest air is located at lower altitudes and downstream of the sting jet. From figure 15, 16 and 17, this is unlikely. Driest air is indeed located downstream of the sting jet but does not show low RH at lower altitudes. Furthermore, the area with low RH is much larger than the length scale of a SJ (in the order of hundreds of kilometres, whereas a sting jet measures a few tens of kilometres in size).

The strong gradient in RH does not coincide with a front. A frontal area marks itself with a gradient in equivalent potential temperature, something which is not visible from modelled data. As such, from this case, but also from theory, SJs are not directly related to a front (i.e. they are not 'front-crossing' features like cold-frontal wind gusts, but are mostly located between the tip of the cloud head and the cold front).

It is more likely that the strong gradient of RH marks the edge of the dry air stream due to the size of the area of low RH and the direction of the latter region.

5.2 RH drop in SJ trajectories

Trajectories provided useful tools in SJ analysis. for instance, the change in RH, altitude and wind speed of a SJ air parcel during a certain period of time could be easily discerned. From theory, sting jets should originate from an area with (nearly) saturated air, i.e. where RH is larger than 90 % (e.g. Clark et al. (2005); L. H. Baker et al. (2014)). All SJs found in this case show these properties, however, some plausible sting jets show lower values of RH at their starting point.

It could be argued that the 'starting point' in this case is not the actual location of origin. Trajectory analysis only went as far back as 00 UTC and before this time, no data is available. For SJs occurring at later times than 06 UTC, another effect blurred the picture of the origin of the Sting jets.

Reinitialisation every six hours leads to small changes in the location and shape of the low pressure system. Although very small, as seen in section 4.1, even the slightest change in the location and shape of the extratropical cyclone can influence the path of a trajectory. On several occasions, hiccups can be discerned from trajectories (figure 18). These 'errors' mostly occur around the tine of reinitialisation. As such, the effect of reinitialisation makes it more difficult to find the origin of a SJ. However, important properties like a drop in RH, altitude and increase in wind speed are still visible and reliable.

It should be noted that RH always decreases when an air parcel descends adiabatically. This could imply that the change in RH is due to the air parcels' descent instead of due to the nature of evaporation inside a SJ. In this case, adiabatic descent partially provides a decrease in RH. However, RH drops more than expected from adiabatic descent alone. The excess of RH drop can probably be attributed to evaporation inside the SJ.

5.3 Sting jets not reaching the surface

Several sting jets have been discerned from cross-sections and trajectories, but it has to be noted that none reach the surface. In other studies, sting jets did descend from aloft to the surface, producing strong gusts (Browning, 2004; Clark et al., 2005; Parton et al., 2009; Martínez-Alvarado et al., 2010, 2014; Smart & Browning, 2014; Browning et al., 2015). In the study of Browning et al. (2015), which covers the same windstorm as this study, SJs were observed to reach the surface. They also concluded that convection and evaporation were important factors for bringing SJ momentum to the surface in this case. Browning et al. (2015) based this on observations as well as a WRF model they've used. It is therefore probable that sting jets should reach the surface in our case study.

Differences between both studies arise in the time period on which the windstorm is modelled. However, observed sting jets are of course not related to a model and can be regarded as instantaneous. Furthermore, horizontal resolution is different (10 km nest in Browning et al. (2015) versus 3 km in this study), as well as the vertical spacing (48 levels versus 70 levels) and spin-up time (24 hours versus a few hours).

A possible answer to the question of sting jets not reaching the surface could be the use of a very high horizontal resolution of 3 km and parametrisation of convection. With high resolutions, as used in this study, convection could probably be resolved directly as we are out of the grey zone. The use of a parametrisation scheme for convection could have resulted in weakened and smeared out convection. When the model would be used to explicitly calculate convection, sting jets would probably have reached the surface.

The latter could provide a solution on why SJs did not reach the surface in this model study. However, it should be noted that Browning et al. (2015) also parametrised convection and in their study, sting jets did reach the surface. Probably, the combination of using a parametrisation scheme on convection or not, combined with a difference in resolution (10 versus 3 km) resulted in sting jets reaching the surface in Browning et al. (2015) and not in this study.

5.4 Evaporation

During most of the rapid-cyclogenetic phase of the extratropical cyclone, evaporation coincides with the area where sting jets were modelled. However, when approaching the final stages of pressure deepening, the evaporative area slowly shifts away from the SJ region. It seems as if the area of strongest evaporation might coincide with the warm sector. A quick reasoning on the latter would point at higher values of moisture content, as warm air can hold more water. In that case, the moisture levels at lower altitudes should be high compared to higher altitudes.

Evaporation was defined as the difference in water content due to phase changes between 700 and 850 hPa. From definition, lower levels were subtracted from higher levels. This leads to a positive value of the amount of phase changed water. If one would do a subtraction for the warm sector between the upper and lower level using the first law of thermodynamics, the result would have a negative sign (i.e. the value of moisture content should be higher at lower levels). Therefore, from this definition, the evaporative area is not directly related to the warm sector. Moreover, the area with highest values of evaporation does not lie completely inside the warm sector, thus decreasing the probability of evaporation being related to the warm sector.

It should be noted that only the phase change of liquid to gas were incorporated in the calculation of evaporation. An implication of this approach could be an offset of a few g/kg. This could furthermore lead to an evaporative area which is smaller than in reality. I.e., cold air on the northern and western side of the low pressure area (cold sector with air of polar origin) would probably contain more ice particles which could 'evaporate' than warm sector air. Some authors use RH with respect to ice to

overcome phase change errors, as well as precipitation entering the sting jet from aloft (e.g. Browning (2004); Clark et al. (2005); Martínez-Alvarado et al. (2013, 2014)

As a stand-alone process, phase-change evaporation seems to partially relate to the SJ, because the area of evaporation is much larger than the region where SJs could occur. This could lead to the conclusion that evaporation is not a consequence of the occurrence of a SJ, but is foremost a precursor for a SJ to develop.

5.5 Conditional Symmetric Instability

The occurrence of CSI was determined using MPV* as proxy. There are several areas of negative MPV*, meaning CSI is possible. The relation between CSI and SJs only applies to the SJ region. When the first SJ emerges, no CSI is present. Only a few hours later CSI and SJs coincide with each other. During the rest of the storm's development, CSI and SJ work alongside each other.

From theory, CSI can provide the right circumstances for a SJ to develop ((Martínez-Alvarado et al., 2013; Gray et al., 2011)). Interestingly, CSI only presents itself after the first SJs have already emerged. This opposes the occurrence of evaporation, which already presented itself before the first SJs developed. Whereas evaporation shifts out of the SJ region when the extratropical cyclone progresses, CSI coincides with the latter area for the remainder of the windstorm. Another difference is that evaporation kicks in earlier than CSI. It could thus be concluded that evaporation is more important during the early stages of an extratropical cyclone, but that the importance of CSI increases as the storm progresses.

The latter applies for this case, which does not mean the same happens in other cases. There is thus some uncertainty whether a decrease in the importance of evaporation is followed by an increasing importance of CSI in general. This question could be addressed by conducting research on the relative importance of evaporation and CSI in many case studies. The latter has not been done in combination with evaporation and frontolysis, however, for instance Gray et al. (2011) already found CSI to be an important factor influencing sting jets in several windstorms. Another possibility would be to conduct an idealised study, in which evaporation and CSI can be controlled. In their idealised study, L. H. Baker et al. (2014) found CSI to be of great importance. Coronel et al. (2016) however concluded that CSI was relatively unimportant and attributed the sting jet to frontolysis.

5.6 Frontogenesis and frontolysis

Frontogenesis and frontolysis derived from modelled data in this case show an incoherent image. Most of the time, frontolysis does not occur inside the SJ region, nor can a clear pattern of frontogenesis be found in fronts which should show increasing frontal strength from theory. Several factors could attribute to these inconsistencies. First of all, Petterssen Frontogenesis analysis was conducted in this case study. Petterssen Frontogenesis, however, only takes frontal developments in the horizontal direction into account. The vertical direction is completely omitted. This could have an effect on the SJ region itself, as processes in that area have a slantwise and thus vertical direction. When not taking this three-dimensional picture into account, frontolysis could be missed in the analysis. This could explain the discrepancy between frontolysis and SJs which were found. However, using Petterssen Frontogenesis instead of a three-dimensional meaasure does not explain the frontolytic features in fronts which should be frontogenetic. In the bent-back occluded front, warm and cold front, processes in the vertical certainly play a role. However, Petterssen Frontogenesis has always proved to be rather reliable for large-scale frontal processes and has been used since the 1930s.

To counter the disadvantages of Petterssen Frontogenesis, analyses with (the divergence of) Q-vectors could be undertaken. The latter method makes use of all spatial dimensions and could thus prove useful in this case. An analysis with Q-vectors has not been done in this case study and as such, a comparison for this case cannot be made. The use of Q-vectors and their divergence have already been proposed by Coronel et al. (2016). In their study, the use of Q-vectors proved to be useful as an analytic method. It is recommended to use Q-vectors instead of Petterssen Frontogenesis in future research on frontolytic effects in sting jets.

A distinct feature is visible in all plots in frontogenesis (figure 21). Ripples occur at the boundaries of all figures. There is a dampening effect on these 'waves' when moving away from the boundaries. In the production of these figures, a method has been used to calculate the horizontal gradients of potential temperature. This method for calculating the derivative in equations 11 and 10 used boundary conditions which would work best on a global grid. In that case, boundaries would not exist. However, when applying this method on a WRF-modelled nest with clear boundaries, errors could have been created. By using this method of horizontal gradient calculation, the formula would need values outside the domain. There are no values, so non-existent numbers have been created at the boundaries. When calculating neighbouring cells, 'wrong' values are used and a wave pattern is created. This luckily dampens out when moving further from the edges of the domain.

Due to this calculation method, an error in the magnitude of values of F was probably created. It is not expected, though, that this largely influenced the sign or magnitude of Petterssen Frontogenesis. Areas of frontogenesis and frontolysis should thus approximately coincide with theoretical regions of frontal development or dissipation. To gain absolute certainty whether this calculation method is the main factor for the unclear picture of frontolysis in the SJ region, an analysis with Q-vectors should be conducted. As this has not been done for this case, the results of frontogenesis and frontolysis could be regarded

as unclear. Therefore, these results have not been taken into account in the analysis of relative importance of evaporation, CSI and frontolysis.

5.7 The effect of reinitialisation

The use of reinitialisation the model every six hours has proved useful on several occasions. The St. Jude's Day storm was modelled well compared to observations. Furthermore, sting jets have been found at the same location and time as modelled and observed by Browning et al. (2015). The high model performance reached due to reinitialisation in this case-study also had several drawbacks. First of all, all high-res data has to be calculated again after reinitialising, i.e. the model does not perform as a 3 km resolution model due to spin-up in the first hours. Moreover, a comparison between data of the non-reinitialised run could not be compared to the reinitialised run, since the run has been stopped after six model hours. To improve comparison results, the model should have been run longer, while reinitialising every six hours.

6 Conclusion

The St. Jude's Day storm of 28 October proved to be a vigorous gale, accounting for several casualties and large damages. Wind gusts of 150-190 km/h were observed, as well as hurricane force winds. A case study has been conducted on this storm with WRF, using nests with a horizontal resolution of 3 km. The model has been reinitialised with ECMWF model data every six hours. The model performed well and the resulting output was very close to observations.

The storm track and core pressure were almost similar in model data and observations. Lowest pressure was reached at approximately 12 UTC with 968 hPa in both observations and model. Sting jets were observed above southern England and also modelled in the same area. SJs were found in model data from 00 UTC to 15 UTC. During the last hours if this time period, the number of SJs slowly decreased. After 15 UTC, no sting jets have been discerned from model data.

Most SJs occurred between 3000 and 2000 m. Trajectory analysis revealed an increase in wind speed from 5 m/s to approximately 40 m/s in descending SJ air parcels. Furthermore, RH humidity decreased strongly.

Distinct areas of evaporation have been discerned from model data and coincide with the sting jet region. Strongest evaporation shifts away from the latter area during the final stage of rapid cyclogenesis. CSI occurred a few hours later than evaporation, but remained in the SJ region for the remainder of the storm. As such, evaporation is relatively more important in the early sting jet phase, becoming less important when the storm progresses. The relative importance of CSI increases as the storm moves further north-eastwards. In conclusion, a sequence of evaporation, followed by CSI affects modelled sting jets in this case study.

The importance of frontolysis could not be assessed, because of unclear results. Frontolytic areas were visible in frontal areas which should be frontogenetic. Frontolysis only coincides with the SJ region in a couple of cases. The use of Petterssen Frontogenesis for the analysis could provide an answer to the discrepancies between theory on the location of frontolysis and modelled frontolytic areas. The use of Q-vectors could be used to overcome the latter, as Q-vectors make use of three spatial dimensions, whereas Petterssen frontogenesis only uses two horizontal dimensions.

Figures on frontogenesis showed a ripple effect at the boundaries. This could be related to the use of a derivation method which should be applied on a global grid. As the nest on which this formula is applied has fixed boundaries, the result could be erroneous. However, the errors produced probably have not changed the magnitudes or sign of values of F in the centre part of the figures.

As computer power increases, future research can focus on the use of very high-res domains, without using nests. This could lead to ability to follow sting jets better, without discrepancies in storm track and overall shape of the extratropical cyclone induced by reinitialisation. However, reinitialising could still be useful, since models tend to shift away from reality over time.

It is recommended to always conduct trajectory analyses in research on SJs, since a two-dimensional spatial picture does not give enough information. Trajectories provide exact values on several parameters in a spatial and temporal domain. The use of clustered instead of singe trajectories could further improve the analysis of the origin of sting jet air parcels.

Finally, further research should be conducted on the sequence of events and relative importance of evaporation, CSI and frontolysis in new case studies, as well as idealised studies. Doing this for the life-cycle of an extratropical cyclone could improve our understanding on sting jets, improve models and subsequently weather forecasts.

7 Acknowledgements

I would like to acknowledge Kees van den Dries for helping with the set-up of Lagranto. Without his help, trajectory analysis would never have been possible. I would also like to acknowledge Gert-Jan Steeneveld and Leo Kroon for providing the opportunity of doing research on a subject which is uncommon in Wageningen. Finally, I would like to thank Lars van Galen for providing some information (presentation slides from a course at ETH) on sting jets. I furthermore would like to thank him for our regular in-depth discussions on (sting jet related) physics.

8 Appendices

8.1 Appendix A: table of variables

Table 2: Table of variables. Variables in this table occur in order of appearance in the main text

variable	Name	Standard value (optional)	Unit
q	Specific heat energy		$J\ kg^{-1}$
c_p	Specific heat capacity of dry air at constant pressure	1005	$J\ kg^{-1}\ K^{-1}$
T	Temperature		K
ρ	Density of air		$kg\ m^{-3}$
p	Air pressure		Pa
L_v	Latent heat of vaporization	2.501E6	$J\ kg^{-1}$
q_s	Water saturation specific humidity		$kg\ kg^{-1}$
CAPE	Convective Available Potential Energy		$kJ\ kg^{-1}$
R_d	Gas constant for dry air	287	$J\ kg^{-1}\ K^{-1}$
T_v	Virtual temperature		K
r	Mixing ratio		$kg\ kg^{-1}$
ϵ	Ratio of gas constants of dry and moist air	0.622	-
M	Absolute momentum surface component		$m\ s^{-1}$
N	Absolute momentum surface component		$m\ s^{-1}$
f	Coriolis parameter		s^{-1}
Ω	Earth rotation rate	7.292E-5	s^{-1}
ϕ	Latitude		deg
x	Distance in x direction		m
y	Distance in y direction		m
v	Wind in y direction		$m\ s^{-1}$
u	Wind in x direction		$m\ s^{-1}$
MPV^*	Saturated moist potential vorticity		$K\ kg\ m^{-2}\ s^{-1}$
ζ	Relative vorticity		s^{-1}
θ_e^*	Saturated equivalent potential temperature		K
RH	Relative humidity		%
F	Petterssen frontogenesis		s^{-1}
t	Time		s
θ	Potential temperature		K
$\mathbf{Q}$	Q-vector		
g	Gravitational constant	9.81	$m\ s^{-2}$
u_g	Geostrophic wind		$m\ s^{-1}$

References

Baker, L. (2009). Sting jets in severe northern european wind storms. *Weather*, *64*(6), 143–148. doi: 10.1002/wea.397

Baker, L. H., Gray, S. L., & Clark, P. A. (2014, January). Idealised simulations of sting-jet cyclones. *Quarterly Journal of the Royal Meteorological Society*, *140*(678), 96-110. doi: 10.1002/qj.2131

Barredo, J. (2010). No upward trend in normalised windstorm losses in europe. *Nat. Hazards Earth Syst. Sci*, *10*, 97–104.

Bjerknes, J. (1919, February). On the structure of moving cyclones. *Monthly Weather Review*, *47*(2), 95-99. doi: 10.1175/1520-0493(1919)47⟨95:OTSOMC⟩2.0.CO;2

Browning, K. A. (2004, January). The sting at the end of the tail: Damaging winds associated with extratropical cyclones. *Quarterly Journal of the Royal Meteorological Society*, *130*(597), 375-399. doi: 10.1256/qj.02.143

Browning, K. A., Ballard, S. P., & Davitt, C. S. A. (1997). High-resolution analysis of frontal fracture. *Monthly Weather Review*, *125*(6), 1212-1230. doi: 10.1175/1520-0493(1997)125⟨1212:HRAOFF⟩2.0.CO;2

Browning, K. A., Smart, D. J., Clark, M. R., & Illingworth, A. J. (2015, October). The role of evaporating showers in the transfer of sting-jet momentum to the surface. *Quarterly Journal of the Royal Meteorological Society*, *141*(693), 2956-2971. doi: 10.1002/qj.2581

Carlson, T. N. (1980, October). Airflow Through Midlatitude Cyclones and the Comma Cloud Pattern. *Monthly Weather Review*, *108*(10), 1498-1509. doi: 10.1175/1520-0493(1980)108⟨1498:ATMCAT⟩2.0.CO;2

Clark, P. A., Browning, K. A., & Wang, C. (2005, July). The sting at the end of the tail: Model diagnostics of fine-scale three-dimensional structure of the cloud head. *Quarterly Journal of the Royal Meteorological Society*, *131*(610), 2263-2292. doi: 10.1256/qj.04.36

Cohen, R. A., & Schultz, D. M. (2005). Contraction rate and its relationship to frontogenesis, the lyapunov exponent, fluid trapping, and airstream boundaries. *Monthly Weather Review*, *133*(5), 1353-1369. doi: 10.1175/MWR2922.1

Coronel, B., Ricard, D., Rivière, G., & Arbogast, P. (2016, April). Cold-conveyor-belt jet, sting jet and slantwise circulations in idealized simulations of extratropical cyclones. *Quarterly Journal of the Royal Meteorological Society*, *142*(697), 1781-1796. doi: 10.1002/qj.2775

Donat, M., Leckebusch, G., Wild, S., & Ulbrich, U. (2011). Future changes in european winter storm losses and extreme wind speeds inferred from gcm and rcm multi-model simulations. *Natural Hazards and Earth System Sciences*, *11*(5), 1351.

Gray, S. L., Martínez-Alvarado, O., Baker, L. H., & Clark, P. A. (2011, July). Conditional symmetric instability in sting-jet storms. *Quarterly Journal of the Royal Meteorological Society*, *137*(659), 1482-1500. doi: 10.1002/qj.859

Grønås, S. (1995, October). The seclusion intensification of the New Year's day storm 1992. *Tellus A*, *47*(5), 733-746. doi: 10.1034/j.1600-0870.1995.00116.x

Hoskins, B. J., Draghici, I., & Davies, H. C. (1978). A new look at the omega-equation. *Quarterly Journal of the Royal Meteorological Society*, *104*(439), 31–38. doi: 10.1002/qj.49710443903

Leckebusch, G. C., & Ulbrich, U. (2004). On the relationship between cyclones and extreme windstorm events over europe under climate change. *Global and planetary change*, *44*(1), 181–193.

Martínez-Alvarado, O., Baker, L. H., Gray, S. L., Methven, J., & Plant, R. S. (2014, April). Distinguishing the Cold Conveyor Belt and Sting Jet Airstreams in an Intense Extratropical Cyclone. *Monthly Weather Review*, *142*(8), 2571-2595. doi: 10.1175/MWR-D-13-00348.1

Martínez-Alvarado, O., Gray, S. L., Catto, J. L., & Clark, P. A. (2012, May). Sting jets in intense winter North-Atlantic windstorms. *Environmental Research Letters*, *7*(2), 024014. doi: 10.1088/1748-9326/7/2/024014

Martínez-Alvarado, O., Gray, S. L., Clark, P. A., & Baker, L. H. (2013, March). Objective detection of sting jets in low-resolution datasets. *Meteorological Applications*, *20*(1), 41-55. doi: 10.1002/met.297

Martínez-Alvarado, O., Weidle, F., & Gray, S. L. (2010). Sting jets in simulations of a real cyclone by two mesoscale models. *Monthly Weather Review*, *138*(11), 4054-4075. doi: 10.1175/2010MWR3290.1

Parton, G. A., Vaughan, G., Norton, E. G., Browning, K. A., & Clark, P. A. (2009, April). Wind profiler observations of a sting jet. *Quarterly Journal of the Royal Meteorological Society*, *135*(640), 663-680. doi: 10.1002/qj.398

Petterssen, S. (1936). Contribution to the theory of frontogenesis. *Geofysiske Publikasjoner*, *11*(6), 1-27.

Schultz, D. M. (2001, September). Reexamining the Cold Conveyor Belt. *Monthly Weather Review*, *129*(9), 2205-2225. doi: 10.1175/1520-0493(2001)129⟨2205:RTCCB⟩2.0.CO;2

Schultz, D. M., & Browning, K. A. (2017). What is a sting jet? *Weather*, *72*(3), 63–66.

Schultz, D. M., Keyser, D., & Bosart, L. F. (1998). The effect of large-scale flow on low-level frontal structure and evolution in midlatitude cyclones. *Monthly*

Weather Review, *126*(7), 1767-1791. doi: 10.1175/1520-0493(1998)126⟨1767:TEOLSF⟩2.0.CO;2

Schultz, D. M., & Sienkiewicz, J. M. (2013, March). Using Frontogenesis to Identify Sting Jets in Extratropical Cyclones. *Weather and Forecasting*, *28*(3), 603-613. doi: 10.1175/WAF-D-12-00126.1

Schultz, D. M., & Vaughan, G. (2010, December). Occluded Fronts and the Occlusion Process: A Fresh Look at Conventional Wisdom. *Bulletin of the American Meteorological Society*, *92*(4), 443-466. doi: 10.1175/2010BAMS3057.1

Schwierz, C., Köllner-Heck, P., Zenklusen Mutter, E., Bresch, D. N., Vidale, P.-L., Wild, M., & Schär, C. (2010). Modelling european winter wind storm losses in current and future climate. *Climatic change*, *101*(3), 485–514.

Shapiro, M., & Keyser, D. (1990). Fronts, jet streams and the tropopause. In C. Newton & C. Holopainen (Eds.), *Extratropical Cyclones, The Erik Palmén Memorial Volume* (p. 167-191). Amer. Meteor. Soc.

Shutts, G. J. (1990, October). Dynamical aspects of the october storm, 1987: A study of a successful fine-mesh simulation. *Quarterly Journal of the Royal Meteorological Society*, *116*(496), 1315-1347. doi: 10.1002/qj.49711649604

Skamarock, W. C., & Klemp, J. B. (2008). A time-split nonhydrostatic atmospheric model for weather research and forecasting applications. *Journal of Computational Physics*, *227*(7), 3465–3485.

Smart, D. J., & Browning, K. A. (2014, January). Attribution of strong winds to a cold conveyor belt and sting jet. *Quarterly Journal of the Royal Meteorological Society*, *140*(679), 595-610. doi: 10.1002/qj.2162

Sprenger, M., & Wernli, H. (2015, August). The LAGRANTO Lagrangian analysis tool – version 2.0. *Geoscientific Model Development*, *8*(8), 2569-2586. doi: 10.5194/gmd-8-2569-2015